Atmos. Chem. Phys. Discuss., 9, 11699–11751, 2009
www.atmos-chem-phys-discuss.net/9/11699/2009/

Atmospheric Chemistry and Physics Discussions

This discussion paper is/has been under review for the journal *Atmospheric Chemistry and Physics (ACP)*. Please refer to the corresponding final paper in *ACP* if available.

Investigation of ship-plume chemistry using a newly-developed photochemical ship-plume model

H. S. Kim, R. S. Park, and C. H. Song

Department of Environmental Science and Engineering, Gwangju Institute of Science and Technology (GIST), Gwangju, Korea

Received: 14 April 2009 – Accepted: 2 May 2009 – Published: 12 May 2009

Correspondence to: C. H. Song (chsong@gist.ac.kr)

Published by Copernicus Publications on behalf of the European Geosciences Union.

Abstract

A photochemical ship-plume model, which can consider the ship-plume dynamics and ship-plume chemistry, simultaneously, was developed to gain a better understanding of atmospheric impact of ship emissions. The model performance was then evaluated by a comparison with the observation data measured on a NOAA WP-3D flight during the Intercontinental Transport and Chemical Transformation 2002 (ITCT 2K2) airborne field campaign. The simulation conditions and parameters, such as meteorological conditions, emission rates, and background gas and particulate species concentrations, were obtained directly and/or inferred indirectly from the ITCT 2K2 observation data. The model-predicted concentrations showed good agreement with the observed concentrations of five ambient species (NO_x, NO_y, O_3, HNO_3, and H_2SO_4) at the eight plume transects by the WP-3D flight with strong correlations around the 1:1 line ($0.66 \leq R \leq 0.85$). In addition, a set of tests were carried out to approximate the magnitude of the reaction probability of HNO_3 onto sea-salt particles in the model-observation comparison framework. These results suggest that the reaction probability of HNO_3 onto sea-salt particles may be in the order of 10^{-3} or smaller. The equivalent NO_x lifetime throughout the "entire" plume was also estimated from ship-plume chemistry modeling. The NO_x lifetimes estimated throughout the "entire ship plume" was 3.36 h. The short NO_x lifetime over the entire ship plume clearly shows that the ship-plume chemistry shortens the NO_x lifetime considerably. Therefore, the ship-plume chemistry model should be used to model the changes in ship-plume chemical compositions and better evaluate the atmospheric impact of ocean-going ship emissions.

1 Introduction

Ocean-going ship emissions are considered important contributors to climate change and atmospheric environmental pollution in the marine boundary layer (MBL). This importance has been recognized since the late 1990s (Corbett and Fishbeck, 1997;

ACPD

9, 11699–11751, 2009

Capaldo et al., 1999; Corbett et al., 1999; Lawrence and Crutzen, 1999). Corbett and Fishbeck (1997) and Corbett et al. (1999) first estimated the annual global emission fluxes of SO_2 and NO_x from ocean-going ships. They estimated that global NO_x and SO_2 emission fluxes in 1993 were 10.12 ($Tg\,yr^{-1}$) and 8.48 ($Tg\,yr^{-1}$), respectively. Since then, the NO_x and SO_2 emission fluxes from ocean-going ships have been further updated and re-evaluated using more sophisticated ship-emission estimation methodologies and updated fuel combustion data (Corbett and Koehler, 2003; Endresen et al., 2003; Beirle et al., 2004). For example, Beirle et al. (2004) estimated the NO_x emission fluxes from ocean-going ships over the Indian Ocean, using the GOME-derived NO_2 vertical column density. Corbett and Koehler (2003) updated the global ship emission data using updated fuel consumption data for 2001. Based on Corbett and Koehler's estimation (2003), NO_x and SO_2 emissions contribute approximately ~21% and ~7% of the total global NO_x and SO_2 emissions from fuel combustion. Although ship SO_2 emissions comprise ~7% of the global SO_2 emissions, it is a dominant source of SO_2 within the MBL, and may produce significant amounts of non-sea-salt (nss) sulfate (Capaldo et al., 1999). The increased amount of nss-sulfate can further enhance the production of cloud condensation nuclei (CCN) within the remote MBL, resulting in a negative global radiative forcing of $\sim -0.11\,Wm^{-2}$ (Capaldo et al., 1999; Phinney et al., 2009). Lawrence and Crutzen (1999) examined the perturbation effects of ocean-going ship-emitted NO_x on the oxidation cycles in the ship-going MBL. They found from a 3-D Eulerian Chemistry-Transport modeling (CTM) study that the ozone and OH radical concentrations were elevated by a factor of ~2 and ~5, respectively, when the ocean-going ship emissions were taken into account. However, their predictions overestimated the NO_x, O_3, and OH levels within the remote MBL (Kasibhatla et al., 2000; Davis et al., 2001; Song et al., 2003a; von Glasow et al., 2003). Several field observations also showed elevations of the ozone and OH levels in the MLB affected by ocean-going ship emissions (e.g., Davis et al., 2001; Chen et al., 2005). More recently, Endersen et al. (2003) estimated the global net radiative forcing from ship emissions using a global CTM (Oslo CTM2), and the net radiative forcing ranged from 0.01 to

0.02 (Wm^{-2}) but with considerable uncertainty. On the other hand, the emissions of particulate species from ocean-going ships can also affect the radiative forcing over ocean areas, while particles playing the important role of cloud condensation nuclei (CCN) in the formation of marine stratiform clouds (Radke et al., 1989; Twomey, 1997; Ferek et al., 1998; Russell et al., 1999; Hudson et al., 2000), which are often called "ship tracks". Overall, NO_x, SO_2, and particle emissions from ocean-going ships significantly affect the atmospheric oxidation cycles within the MBL and global radiation budget, even though there is still large uncertainty in their quantitative estimations.

As mentioned above, it was reported that the use of the coarse-grid 3-D CTMs in treating point-source emissions, such as ships, could lead to over-predictions in the NO_x, O_3 and OH levels (Kasibhatla et al., 2000; Davis et al., 2001; Song et al., 2003a; von Glasow et al., 2003; Chen et al., 2005), by skipping the nonlinear ship-plume chemistry. For example, Song et al. (2003a) focused on in-plume chemical transformations using a plume-chemistry model. Their study demonstrated the importance of taking the ship-plume chemistry into account when determining the NO_x, O_3, and OH concentrations. von Glasow et al. (2003) also suggested that the absence of nonlinear ship-plume chemistry can result in over-predictions in the NO_x, O_3, and OH levels. However, these studies have limitations in that the model investigations were carried out based on a simple 0-dimensional Lagrangian photochemical box model without any model validation with observations. Although Chen et al. (2005) examined the ship-plume chemistry with plume observation data from the ITCT 2K2 aircraft campaign and the predicted atmospheric concentrations from photo-stationary state modeling, their study may also have a limitation in that the model used in their study was not a full ship-plume chemistry model. Rather, it was a general photo-stationary state model constrained by the observed atmospheric species concentrations. Therefore, their model could not predict the concentrations over the "entire volume" of the ship plume.

The development of the "entire volume" ship-plume model is important because the ship-plume photo-chemistry is highly non-linear, not only "along the plume-advecting

direction" (x-direction), but also "in the plume-dispersing direction" (y- and z-directions). In addition, the distributions of the ship-plume species concentrations in the y- and z-directions are frequently "non-Gaussian", particularly for secondarily-formed species, such as ozone and OH. The present study developed a ship-plume chemistry model that can explicitly consider the "non-linear" and "non-Gaussian" characteristics of chemical evolution of the "entire" ship plume (Sect. 2). The data from the developed ship-plume photochemistry model was compared with aircraft observation data from the ITCT 2K2 campaign (Sect. 3). Section 4 evaluates the magnitude of the reaction probability of HNO_3 onto sea-salt particles ($\gamma_{HNO_3,ss}$), which is a currently "hotly-debated issue". Subsequently, using the developed ship-plume photochemistry model, NO_x chemical lifetimes ($\tau^{chem}_{NO_x}$) were estimated over the "entire" ship plumes (Sect. 5). The estimation of $\tau^{chem}_{NO_x}$ is important, for example when the NO_x emission fluxes from ships are estimated from the satellite-retrieved NO_2 columns over the ship-going oceans, as conducted by Beirle et al. (2004).

2 Model development

2.1 Ship-plume chemistry

In this study, we developed UBoM 2K8 model (Utility photochemical Box Model 2K8). Since the UBoM 2K8 model was first developed, it has been applied to three different types of atmospheric chemistry modeling study: (i) Lagrangian backward/forward trajectory photochemical modeling (Song et al., 2007), (ii) Eulerian photochemical box modeling, and (iii) ship-plume chemistry modeling (Song et al., 2003a, b). Although it has been operated in the three different modes, the three modes share the same atmospheric photochemical components, heterogeneous parameterizations and aerosol chemistry of the UBoM 2K8 model.

The photochemical components of the UBoM 2K8 model are the same as those used in previous studies (e.g., Crawford et al., 1999; Song et al., 2003a, b, 2007). The cur-

ACPD
9, 11699–11751, 2009

rent model mechanism includes 71 H_xO_y-N_xO_y-CH_4 related reactions and 184 NMHC reactions. The former chemistry is based on Lurmann et al.'s (1986) condensed mechanism with some major modifications. These include appropriately updated rate coefficients as well as additional NO_x and organic peroxide reactions (e.g., Atkinson et al., 1997; DeMore et al., 1997; Crawford et al., 1999). In addition to these gas-phase photochemical reactions, several gas/aqueous-phase sulfur reactions/equilibria were also included to examine the chemical fates of the various sulfur species in the atmosphere (Song et al., 2003b). The gas-particle interactions between nitrate precursor species (N_2O_5, NO_3, and HNO_3) and aerosols were considered using pseudo-first order kinetics:

$$\frac{d[C_i]}{dt} = -k_{mt,i}[C_i] \quad (1)$$

where $[C_i]$ is the concentration of gas-phase species "i", and $k_{mt,i}$ is the overall mass transfer coefficient (s^{-1}). The Schwartz formula to calculate $k_{mt,i}$ for the precursor species of nitrate (Schwartz, 1986) was used:

$$k_{mt,i} = \frac{\gamma_i S \overline{v_i}}{4} \quad (2)$$

where γ_i represents the reaction probability (or uptake coefficient) of the precursor species "i", S is the aerosol surface density ($cm^2\,cm^{-3}$), and $\overline{v_i}$ is the molecular mean velocity ($cm\,s^{-1}$) of the precursor species "i". In particular, using Eqs. (1) and (2), a parameterization for HNO_3 partitioning onto atmospheric aerosols was added to the UBoM 2K8 model, which had not been considered explicitly in previous studies (Song et al., 2003a, b; Chen et al., 2005; Song et al., 2007).

In order to consider the interactions between sulfate precursor species (SO_2 and H_2SO_4) and sea-salt particles, the following parameterization was used to account for the precursor accommodation and aqueous-phase oxidation reactions of SO_2 in sea-

salt particles (Brasseur et al., 1999; Mari et al., 1999; Song et al., 2003b):

$$\frac{1}{k_{t,\mathrm{SO_2}}} = \frac{1}{k_{mt,\mathrm{SO_2}}} + \frac{1}{k_{\mathrm{O_3}} + k_{\mathrm{H_2O_2}}} \quad (3)$$

where $k_{t,\mathrm{SO_2}}$ represents the total (or net) SO_2 scavenging and oxidation loss coefficient (s^{-1}); and $k_{\mathrm{O_3}}$ and $k_{\mathrm{H_2O_2}}$ denote the overall oxidation rate coefficients (s^{-1}) by aqueous O_3 and H_2O_2, respectively. For the condensation of SO_2 and H_2SO_4, $k_{mt,i}$ and γ_i are replaced by $k_{t,i}$ and α_i (mass accommodation coefficient) in Eqs. (1) and (2), respectively. More details on the parameterizations can be found in the report by Song et al. (2003b).

The photolysis rate coefficients used are those based on a DISORT 4-stream implementation of the NCAR Tropospheric Ultraviolet-Visible (TUV) radiative code with an updated $O(^1D)$ quantum yield (Talukdar et al., 1997). The solutions to the ordinary differential equations that describe the time-dependent variations in atmospheric species concentrations were achieved using the Gear ODE (Ordinary Differential Equation) solver.

2.2 Ship-plume dynamics

The fundamentals of the plume transport and turbulent dispersion are based on Hanna et al. (1985)'s Offshore and Coastal Dispersion (OCD) algorithm. The plume centerline concentration of species "*i*" can be expressed as follows:

$$\frac{C_i}{Q_i} = \frac{1}{\pi u_r \sigma_y \sigma_z} \quad (4)$$

where Q_i is the emission rate ($kg\,s^{-1}$) of the primary pollutant species "*i*" from the ship, u_r is resulting wind speed, which is related to the relative motion of the ship and wind; and σ_y and σ_z represent the lateral and vertical turbulent dispersion parameters, respectively. Many meteorological variables are necessary to correctly determine σ_y and

ACPD
9, 11699–11751, 2009

σ_z, such as the standard deviations for the lateral and vertical fluctuation parameters, friction velocity (u_*), and surface roughness length (z_o). Previously, Song et al. (2003a) derived some useful expressions for σ_y and σ_z as a function of the downwind distances (x) and atmospheric stability classes. These formulas (or methodology) were applied to the current study with some extensions. The formulas used in this study are shown in Table 1.

As mentioned previously, the basic concept of the newly-developed ship-plume photochemical model is the same as that reported by Song et al. (2003a, b). Figure 1a shows a schematic diagram of the dynamic plume development due to turbulent dispersion. In the course of plume development, the plume is dispersed elliptically at the y-z plane, as shown in Fig. 1a. In case that the boundary layer is capped by the "inversion height" (or "mixing height"; denoted as h in the z-direction), it was assumed that the plumes cannot be dispersed above the mixing height. At this point, σ_z is not allowed to expand beyond approximately 0.8 h. Therefore, in this case, dispersion takes place only in the y-direction (refer to Fig. 1b). Based on this, the dilution factors for species "i" ($D_{i,k}$) were defined using the following equations (Song et al., 2003a):

$$D_{i,k} = \frac{C_{i,k+1}}{C_{i,k}} = \frac{(\sigma_y \sigma_z)_k}{(\sigma_y \sigma_z)_{k+1}}, \text{ if } \sigma_z \le 0.8\,h \tag{5}$$

$$D_{i,k} = \frac{C_{i,k+1}}{C_{i,k}} = \frac{(\sigma_y)_k}{(\sigma_y)_{k+1}}, \text{ if } \sigma_z > 0.8\,h \tag{6}$$

where $C_{i,k}$ and $C_{i,k+1}$ denote the concentration of species "i" at the time steps k and $k+1$, respectively (see Fig. 1a and b). The value of $D_{i,k}$ is always between 0 and 1. This dilution factor can be understood as a ratio of the elliptical plume areas at the y-z plane during Δt. Therefore, the change in concentration of species "i" (ΔC_i^D) due to atmospheric turbulent dispersion (or dilution) can be expressed by:

$$\Delta C_i^D = C_{i,k+1} - C_{i,k} = \left(D_{i,k} - 1\right) C_{i,k} + \left(1 - D_{i,k}\right) C_{i,b} \tag{7}$$

ACPD
9, 11699–11751, 2009

Here, $C_{i,b}$ indicates the background (out-plume) concentration of species "*i*".

In order to predict the plume concentrations throughout the entire ship plume, it was assumed that the concentrations of primary pollutants, such as NO_x and SO_2, are distributed along the y-z plane, with Gaussian shapes (refer to Fig. 1a and b):

$$\xi(\chi, t) = \frac{1}{\sqrt{2\pi}\sigma(t)} \exp\left[\frac{-\chi^2}{2\sigma(t)^2}\right] \quad (8)$$

where $\xi(\chi, t)$ represents the Gaussian function at plume-travel time "*t*" and the location χ, χ indicates the distance (deviation) from the plume center (i.e., y=0 and z=0) on the y and/or z planes, $\sigma(t)$ denotes the standard deviation (or dispersion parameter) at plume-travel time "*t*", which was determined by the formulas in Table 1. Hence, the primary pollutant distributions can be calculated from Eqs. (9) and (10):

$$F_c(\chi, t) = \exp\left[\frac{-\chi^2}{2\sigma(t)^2}\right] \quad (9)$$

$$C_i(\chi, t) = C_{i,cl} F_c(\chi, t) \quad (10)$$

where $F_c(\chi, t)$ is the frequency function, $C_i(\chi, t)$ is the concentration of the primary pollutant i (such as NO_x or SO_2) in a given location χ at plume-travel time t, and $C_{i,cl}$ is the centerline concentration of species i at plume-travel time t. From Eqs. (9) and (10), the peak (or centerline) concentrations of NO_x and SO_2 occur at χ=0. The plume concentrations were calculated over the "entire" ship plume by running the multiple Lagrangian plume boxes along the different σ lines, with 0.25σ increments, as shown briefly in Fig. 1c. At the Lagrangian plume runs, the ship-plume chemistry is driven primarily by the primary pollutant concentrations, which have Gaussian shapes. The levels of the secondary pollutants (e.g., ozone, HNO_3, PAN, NO_3, N_2O_5, and OH) were determined by both the ship-plume photochemistry and ship-plume dynamics, as described previously. The results from the multiple Lagrangian plume runs were smoothed on the y and z planes at each time step. The model calculations were then

ACPD
9, 11699–11751, 2009

forwarded toward the next calculation time step (i.e., time marching), until the ship plume had been diluted completely.

This modeling study can be distinguished from the work by Chen et al. (2005): (i) the model-predicted species concentrations in this study were not the solutions from a photo-stationary state approximation (i.e., dc/dt=0), and (ii) the model calculations were not made with any constraint with the observation data. Photo-stationary state approximations with the constraints of the observation data can produce satisfactory estimates for short-lived species at the locations where the observation data is available. However, it cannot provide adequate solutions for the long-lived and short-lived species concentrations at other ship-plume locations where the observation data are unavailable. In addition, constraining the photo-stationary state modeling with simultaneously observed plume concentrations would be difficult because the observation data for atmospheric species measured by aircraft campaign may have different measurement times and resolutions inside the ship plume. Therefore, in this study, a full ship-plume chemistry modeling was carried out with full time integration, starting with the initial and background chemical and meteorological conditions and ship emission rate, as performed by Karamchandani et al. (2000) for a study of the Cumberland power plant plume during the Southern Oxidant Study (SOS).

3 Model evaluations

3.1 Observations from ITCT 2K2

The simulation performance of the newly-developed photochemical ship-plume model was evaluated by carrying out a comparison study using the observation data from the ITCT 2K2 airborne field campaign. Among the ITCT 2K2 observation data, this study used the data from a ship-plume experiment conducted approximately noon on 8 May, 2002, by a NOAA WP-3D flight. Figure 2 shows the sampling trajectory of the NOAA WP-3D flight. As shown in Fig. 2, the NOAA WP-3D traversed the ship plume eight

times from transects A to H, (Chen et al., 2005). As also shown in Fig. 2, the NOAA WP-3D flight did not traverse the ship plume perpendicularly. The angle between the ship-plume travel and the WP-3D flight path was approximately 59°. The simulation conditions and parameters, such as the meteorological conditions, emission rates, and background gas and particulate species concentrations, were obtained directly and/or inferred indirectly from the ITCT 2K2 observation data. The wind velocity and direction were reported to be 9–11 ($m\,s^{-1}$) and SSE, respectively. The ship was heading WNW, and its speed was ~5 $m\,s^{-1}$ (~9.7 knots) (Chen et al., 2005). During the WP-3D flight experiment, the sky was found to be clear (see Table 2). Information on the sampling instruments is summarized in other publications (Brock et al., 2000, 2003; Nowak et al., 2004; Parrish et al., 2004). Therefore, they are not reported in this manuscript.

3.2 Determination of stability class and modeling conditions

As discussed in Sect. 2.2 and shown Table 1, the turbulent dispersion parameters, σ_y and σ_z, are a strong function of the atmospheric stability. Therefore, two independent meteorological datasets, (i) meteorological data measured by the NOAA WP-3D flight and (ii) NCEP 6 hourly reanalysis-2 pressure-level data, were used to determine the stability classes of the MBL within which the NOAA WP-3D ship-plume measurements had been taken. The three rectangular points in Fig. 2 (I, II, and III), represent the locations where the NECP 6 hourly reanalysis-2 pressure-level data were obtained. Figure 3a and b shows the vertical temperature profiles obtained from the WP-3D flight observations and NCEP reanalysis data, respectively. Figure 3b shows the temperature profiles over the three locations (I, II, and III). The NCEP data obtained at 11:00 a.m. on 8 May, 2002 (when the WP-3D aircraft began to measure the plume composition), were applied to this analysis. Based on the two temperature profiles, the actual lapse rates of air temperature (Γ; $K\,km^{-1}$) were derived from the sea surface to 800 m a.s.l. The Γ from the WP-3D aircraft observations ranged from −3.13 ($K\,km^{-1}$) to −1.09 ($K\,km^{-1}$), and the values of Γ from the NCEP reanalysis data were −0.92 ($K\,km^{-1}$), −0.63 ($K\,km^{-1}$), and −0.34 ($K\,km^{-1}$) for locations I, II, and III, respectively.

ACPD
9, 11699–11751, 2009

The atmospheric stability classes were then determined by a comparison of the actual lapse rate (Γ) with the moisture adiabatic lapse rates (Γ_s). The values of Γ_s were reported to be $\sim$4 K km^{-1} in warm and humid air masses (about 293 K) in the lower MBL and $\sim$5 K km^{-1} to 6–7 K km^{-1} in the cold air (about 283 K) in the middle of the MBL (Gill, 1982; Holton, 1992). Based on the mean air temperatures of approximately 283 K and 286 K for the ITCT 2K2 data and the NCEP reanalysis data, respectively, it was decided to use Γ_s=−5 K km^{-1} for the ITCT 2K2 data and −4.5 K km^{-1} for the NCEP reanalysis data. From these comparisons (Fig. 3a and b), it was concluded that the most likely atmospheric stability within the MBL exists between moderately stable (E) and stable (F). Therefore, ship-plume photochemical modeling was carried out at these two atmospheric stability classes.

The concentrations of gas-phase primary and secondary pollutants, such as NO, NO_2, NO_y, O_3, CO, CO_2, NMHCs, SO_2, HNO_3, H_2SO_4, were obtained from the NOAA WP-3D observations. Again, detailed information on the instruments used in the flight measurements is discussed elsewhere (Brock et al., 2000, 2003; Nowak et al., 2004; Parrish et al., 2004), and is summarized at http://www.esrl.noaa.gov/csd/ITCT/2k2/P3instruments.shtml. The observed mean background concentrations of the gas-phase species outside the ship plume for NO_x, SO_2, O_3, CO, H_2SO_4, HNO_3, PAN, and C_3H_8 were $\sim$190 pptv, 400 pptv, 40 ppbv, 138 ppbv, 0.4 pptv, 5 pptv, 135 pptv, and 370 pptv, respectively. The aerosol-related variables, such as number, size, and volume concentrations, were measured directly using a combination of an aerosol size spectrometer and white light-scattering methods. The chemical composition of particulate species was measured using a particle-into-liquid sampler coupled with an ion chromatograph (PILS-IC) (Weber et al., 2001; Orsini et al., 2003). Table 2 summarizes the background conditions.

In order to consider atmospheric heterogeneous processes, the values of the reaction probabilities (γ_i) for N_2O_5, NO_3, and HNO_3, mass accommodation coefficients (α_i) for SO_2 and H_2SO_4, and aerosol pH, were obtained from previous reports (Song et al., 2003a, b), and are shown in Table 2. However, the reaction probability of HNO_3

($\gamma_{HNO_3,ss}$) on sea-salt particles was assumed to be 10^{-3}. This study tested the magnitude of $\gamma_{HNO_3,ss}$. The details will be discussed in Sect. 4. As indicated previously by Chen et al. (2005), the averaged surface density (S in Eq. 2) of sea-salt particles in the ship plume was measured to be 90 $\mu m^2\,cm^{-3}$. Of a total of 120 $\mu m^2\,cm^{-3}$, the surface density of 30 $\mu m^2\,cm^{-3}$ was assumed to have originated from direct aerosol emissions from the ship. Therefore, these surface densities were used in Eqs. (1) and (2) to calculate the mass flux from the gas and particulate phases, respectively.

The emission rates were obtained directly from the observed emission factors to reduce the uncertainty in the estimation of the ship-emission rates. Because CO_2 is the principal product, the CO_2 balance could be a useful method for estimating the ship emission rate (Hobbs et al., 2000; Sinha et al., 2003). In general, the ideal reaction formula for complete oxidation in ship diesel powered-engines can be given by:

$$C_xH_y + \left(x + \frac{y}{4}\right) O_2 = xCO_2 + \frac{y}{2}H_2O \qquad \text{(R1)}$$

where the y to x ratio is 1.8 (Tuttle, 1955). From Reaction (R1), the mass ratio of CO_2 to C_xH_y is 3.2. Therefore, the mass flux of CO_2 from fuel combustion is 3.2 times the fuel consumption rate. Chen et al. (2005) reported that the emission factors for NO_x and SO_2 in the ship experiment were 20±8 (gN/kg fuel) and 30±4 (gSO_2/kg fuel) from the ratios of $\Delta NO_x/\Delta CO_2$, and $\Delta SO_2/\Delta CO_2$ with same mass balance (Hobbs et al., 2000; Sinha et al., 2003). The NO_x and SO_2 emission rates were calculated to be 6.25 ($g\,s^{-1}$) and 9.38 ($g\,s^{-1}$), respectively, based on the diesel-powered fuel consumption of a ship (27 ton day^{-1}) (Table 2).

3.3 Observations vs. model-predictions

A comparison study was carried out using the ITCT 2K2 aircraft observation data to evaluate the simulation performance of the newly-developed ship-plume chemistry model. As mentioned previously, the variables for the model simulations, such as emission rates, meteorological conditions, aerosol-related variables and background con-

centrations of the gas and particulate species, were obtained directly or inferred indirectly from the NOAA WP-3D airborne observations. Among the observed atmospheric species, the concentrations of the five species, which include gas-phase primary and secondary pollutants (NO_x, NO_y, O_3, HNO_3, and H_2SO_4), were compared with the model-predicted concentrations. Only the five species concentrations were compared in this study due to the measurement response times of the atmospheric species. Since the WP-3D aircraft traversed the ship plume at very high speeds (~360 km h^{-1}) but the plume widths were relatively narrow (0.47–4.14 km), the volume of in-plume data was limited when the measurement response times of the species are not sufficiently fast. Only the five gas-phase species have sufficiently fast response times, whereas particulate species have longer response times. For example, the PILS-IC instrument has a measurement time resolution of ~4 min. Although SO_2 has a fast measurement response time, it was excluded from this analysis. This is because the SO_2 data measured by the aircraft were so scattered that it is difficult to distinguish the plume shape from the background at the eight ship-plume transects, which was partly due to instrument limitations (refer to Chen et al., 2005). In addition, as mentioned previously, the WP-3D flight traversed the ship plume at an angle of approximately 59°. Therefore, for the purpose of comparison, the model-calculated data was sampled along the eight cross sections.

Figure 4 shows the comparison results of NO_x from transects A to H. As discussed in Sect. 3.2, the most likely atmospheric stability class of the MBL would be between moderately stable (E) and stable (F). Therefore, these two stability classes were chosen for the modeling conditions. As shown in Fig. 4a to h, the concentrations of NO_x ($\equiv NO+NO_2$) decreased continuously due to turbulent dispersion (or dilution) and atmospheric photochemical transformation. As shown in Fig. 4, the newly-developed ship-plume photochemical model captures the observed concentrations reasonably well. As expected, the levels of NO_x presented by the dashed lines (stable class F) were higher than those by the solid lines (moderately stable class E) due to less active turbulent dispersion in the stable class.

Although there was good agreement between observed and model-generated concentrations, there was a relatively large discrepancy in plume transect A. As the plume ages, there is a decrease in differences between the observed and model-predicted concentrations. The two possible causes of such discrepancies are: (1) influence of air motion caused by flight movement and (2) effect of other polluted plumes. When the ship plume is fresh, it is easy to distort the plume shape by air motion. However, the possible deformation effects of the plume concentration were decreased with plume aging. In addition, as suggested by Chen et al. (2005), the initial location of the ship experiment is a moderately polluted area. Therefore, the plume concentrations can be affected by other pollution sources. However, again the discrepancies are reduced when ship plume is fully developed.

Figure 5 shows the model-predicted and observed NO_y concentrations. Here, NO_y is defined as $NO+NO_2+NO_3+2N_2O_5+HNO_3+HONO+HNO_4+PAN+NO_3^-$+Organic nitrates. Again, there were relatively large discrepancies in the early plume aging steps, which decreased as the plumes aged photochemically and dynamically. Because most of the NO_y is occupied by NO_x, the differences between the observed and model-predicted NO_y concentrations are similar to those of NO_x.

Figures 6 to 8 show the comparison results for secondary gas-phase pollutants: O_3, HNO_3, and H_2SO_4. As shown in Fig. 6, the newly-developed ship-plume photochemical model captures the atmospheric O_3 chemistry greatly. In the early plume development stages (Fig. 6a and b), the O_3 levels are depleted below the background ozone level (40 ppbv) at the plume centerline, whereas they appear to be produced at the edges of the ship plume. These "non-linear" changes in the O_3 concentrations are caused by ozone titration and recovery processes at the ship-plume cross-section.

$$NO + O_3 \rightarrow NO_2 + O_2 \quad \text{(R2)}$$

$$NO_2 + h\nu \rightarrow O(^3P) + NO \quad \text{(R3)}$$

$$O(^3P) + O_2 \xrightarrow{M} O_3 \quad \text{(R4)}$$

ACPD
9, 11699–11751, 2009

When a ship emits a plume, O_3 is titrated instantaneously by NO via Reaction (R2), because 95% of the NO_x emitted from the ships is NO on a mass basis (Hewitt, 2001), and NO is also found in the excessive levels. At the beginning of the plume age, the O_3 concentrations even decreased to almost 0 ppbv (Song et al., 2003a). After ozone titration, the O_3 level was recovered by the photo-dissociation of NO_2 (a temporary storage of ozone) and subsequent O_3 formation process via Reactions (R3) and (R4) as well as by the entrainment of background ozone. As the ship plume develops, the levels of NO_x drop, maintaining Gaussian shapes in the lateral and vertical (y- and z-) directions. Because of these Gaussian distributions, the edges of the ship plumes first enter the O_3 recovery stage (i.e., both Reactions (R3) and (R4) are active in this stage). However, the center of the plume is still in the O_3 titration mode (i.e., Reaction (R2) is dominant). As shown in Fig. 6a and b, this model can clearly capture these "non-linear" O_3 titration-recovery characteristics over the ship-plume cross-sections. This clearly shows why the "entire ship-plume" model is necessary. Further analysis of the non-linear (and non-Gaussian) characteristics of the secondary pollutants, such as hydroxyl radicals (OH), across the ship-plume cross sections will be reported in Sect. 5. After the early plume development stage, the "entire" plume enters the O_3 production mode. In Fig. 6c–h, the O_3 concentrations were higher than the background O_3 concentration of 40 ppbv with Gaussian shapes across the ship-plume cross sections.

Figure 7 shows the observed and model-predicted HNO_3 concentrations. In this comparison, two observation-based HNO_3 concentrations were used: (i) HNO_3 concentrations measured directly by Chemical Ionization Mass Spectrometer (CIMS) (Huey et al., 2004) and (ii) HNO_3 concentrations estimated from the concentrations of total nitrogen oxides (NO_y). The latter was calculated by subtracting the measured NO_x, measured PAN, modeled particulate nitrate (NO_3^-), and modeled organic nitrate concentrations from the measured NO_y concentrations because the major constituents of NO_y are NO_x, HNO_3, PAN, NO_3^-, and organic nitrates (i.e., $[HNO_3] \cong [NO_y]-[NO_x]-[PAN]-[NO_3^-]-[\text{Organic nitrates}]$). Here, the former (directly-measured plume HNO_3 concentrations) was used only as reference data, since they did not show plume shapes

(presumably, Gaussian) along the plume cross sections, as shown in Fig. 7 (see black circles in the panels). Accordingly, the latter HNO_3 concentrations were calculated and introduced in this analysis. In addition, the PAN observation device generated little available data inside the ship plume. Therefore, the measured average PAN concentration of 135 pptv was used in the latter HNO_3 concentration calculations (Chen et al., 2005). In Fig. 7, the value of the reaction probability of HNO_3 onto the sea-salt particle ($\gamma_{HNO_3,ss}$) was assumed to be 10^{-3} (this will be discusses further in Sect. 4).

In this analysis, the model performance (and heterogeneous parameterizations in the model) can be tested in two ways: (i) how close are the estimated HNO_3 concentrations (the latter) to directly-measured HNO_3 concentrations (the former)? and (ii) how close are the model-calculated HNO_3 concentrations to both observation-based HNO_3 concentrations (i.e., the former and the latter HNO_3 concentrations)? As shown in Fig. 7a to h, the model-predicted HNO_3 concentrations (moderately stable case) capture the levels of the latter HNO_3 across the ship-plume cross sections reasonably well, except for the early plume-aging stages, such as transects A and B. Since NO_x is the most abundant species in NO_y, any uncertainty in the observed NO_x will affect the NO_y levels and hence the estimated HNO_3 (the latter) levels in this comparison study. The estimated HNO_3 concentrations (open rectangles and triangles in Fig. 7) were higher than the directly-measured HNO_3 concentrations (open black circles in Fig. 7) before the transect D. This was attributed to the high measured NO_x concentrations from transects A to D. However, from transect E, the estimated HNO_3 concentrations was similar to the directly-measured HNO_3 concentrations with "$\gamma_{HNO_3,ss}$=10^{-3}". (Sect. 4 will examine the influences of relaxation of $\gamma_{HNO_3,ss}$ from 10^{-4} to 10^{-1}). Here, it should also be noted that since the MBL conditions considered in this study had low NMVOC concentrations, the "missing NO_y" may be small (i.e., [directly measured HNO_3]≅[estimated HNO_3], again see panels e–h in Fig. 7) (Finlayson-Pitts and Pitts, 2000).

The atmospheric levels of HNO_3 are controlled by HNO_3 production and destruction processes. The major atmospheric production and destruction processes of HNO_3 in

ACPD
9, 11699–11751, 2009

the MBL are believed to take place via the following reaction schemes:

$$NO_2 + OH \xrightarrow{M} HNO_3 \quad \text{(R5)}$$

$$NO_3 + DMS \rightarrow HNO_3 + \text{products} \quad \text{(R6)}$$

$$HNO_3 + NaCl \xrightarrow{\text{hetero}} NaNO_3 + HCl \quad \text{(R7)}$$

where DMS in Reaction (R6) represents dimethylsulfide, and Reaction (R7) represents the heterogeneous conversion of HNO_3 into particulate nitrate (NO_3^-), which could be associated preferably with Na^+ inside the sea-salt particles. As discussed in Sect. 2.1, this heterogeneous conversion of gas-phase HNO_3 was parameterized, using Schwartz kinetics with $\gamma_{HNO_3,ss}=10^{-3}$ in Fig. 7. Therefore, these comparison studies can provide a good opportunity for testing this parameterization describing the heterogeneous conversion of HNO_3 into sea-salt particles. This issue will be discussed further in Sect. 4.

Figure 8 shows the observed and model-predicted H_2SO_4 concentrations. Although the comparison results between the observed and model-predicted H_2SO_4 levels show good agreement with each other (Fig. 8), the model-predicted H_2SO_4 concentrations were more or less higher than the observed values, particularly at the early plume-development stages, as shown in Fig. 8a and b. More detailed atmospheric species information, such as the OH radical and sulfate concentrations, will be needed to determine the exact causes of these over-predictions. However, the ITCT WP-3D flight OH and sulfate measurements did not have sufficiently fast time resolution. The possible causes of the over-predictions could be: (i) possible overestimations of the OH radical concentrations from the ship-plume photochemical model and (ii) possible uncertainties in H_2SO_4 scavenging process parameterization and/or heterogeneous accommodation coefficient of H_2SO_4 ($\alpha_{H_2SO_4,ss}$). However, the agreements between the observed and model-predicted H_2SO_4 concentrations get improved as the ship plume develops. Although the observed and model-predicted SO_2 and OH concentrations

were not compared in this study, the H_2SO_4 comparisons suggest that our ship-plume photochemical model reproduces both the ship-plume SO_2 and OH concentrations reasonably well. In addition, the parameterizations to describe the heterogeneous conversion of H_2SO_4 into ship-plume particles in this work would be accurate (refer to Sect. 2.1).

Figure 9 shows scatter plots of the model-predicted and flight-observed species concentrations. As discussed previously, the comparisons between the predicted and observed concentrations of the five species show good correlations around the 1:1 line. As shown in Fig. 9a to e, the correlation coefficients (R) with the "moderately stable" and "stable" conditions range between from 0.67 to 0.85, and from 0.66 to 0.83, respectively (except for HNO_3). For further statistical investigations, the following four statistical parameters were introduced for error and bias analyses: (1) Root Mean Square Error (RMSE; absolute error), (2) Mean Normalized Gross Error (MNGE; relative error), (3) Mean Bias (MB; absolute bias), and (4) Mean Normalized Bias (MNB; relative bias).

$$\mathrm{RMSE} = \sqrt{\frac{1}{N}\sum_{1}^{N}(C_{i,\mathrm{Pred}} - C_{i,\mathrm{Obs}})^2} \tag{11}$$

$$\mathrm{MNGE} = \frac{1}{N}\sum_{1}^{N}\left(\frac{\left|C_{i,\mathrm{Pred}} - C_{i,\mathrm{Obs}}\right|}{C_{i,\mathrm{Pred}}}\right) \times 100 \tag{12}$$

$$\mathrm{MB} = \frac{1}{N}\sum_{1}^{N}(C_{i,\mathrm{Pred}} - C_{i,\mathrm{Obs}}) \tag{13}$$

$$\mathrm{MNB} = \frac{1}{N}\sum_{1}^{N}\left(\frac{C_{i,\mathrm{Pred}} - C_{i,\mathrm{Obs}}}{C_{i,\mathrm{Obs}}}\right) \times 100 \tag{14}$$

where $C_{i,\mathrm{Pred}}$ and $C_{i,\mathrm{Obs}}$ denote the predicted and observed concentrations of atmospheric species "i", respectively. The statistical analyses were carried out with the species concentrations within $\pm 2\sigma$ of the ship-plume distributions at the eight transects. The results are summarized in Table 3. The negative values in MBs and MNBs originated from the higher values of the observed NO_x and NO_y in the early plume-development stages. Based on the correlation (Fig. 9) and the error/bias analyses (Table 3), it appears that the moderately stable (E) condition can produce slightly more accurate predicated species concentrations than the stable condition (F). Therefore, "moderately stable" conditions (E) were used for further analyses.

4 Reaction probability of HNO_3 into sea-salt particles

In Sect. 3, the overall model performances were tested by a comparison with the ITCT 2K2 aircraft observation data. With this comparison framework, an attempt was made to evaluate the magnitude of $\gamma_{HNO_3,ss}$. For this evaluation, sensitivity runs were carried out. The magnitude of $\gamma_{HNO_3,ss}$ has been investigated in many laboratory experiments (e.g., Fenter et al., 1994; Laux et al., 1994; Abbatt and Waschewsky, 1998; Davis and Cox, 1998; Guimbud et al., 2002; Ghosal and Hemminger, 2004; Tolocka et al., 2004; Saul et al., 2006; Lui et al., 2007). However, as shown in Table 4, $\gamma_{HNO_3,ss}$ ranges widely from $\sim 10^{-1}$ to $\sim 10^{-4}$. For example, Abbatt and Waschewsky (1998) reported $\gamma_{HNO_3,ss}$ to be >0.2, whereas other groups reported $\gamma_{HNO_3,ss}$ to be $\sim 10^{-4}$ (e.g., Laux et al., 1994; Davis and Cox, 1998). There appears to be large uncertainty in the magnitude of $\gamma_{HNO_3,ss}$. Therefore, it is believed that a determination of $\gamma_{HNO_3,ss}$ using "field-observation data" is imperative. This is the first modeling study to evaluate the magnitude of $\gamma_{HNO_3,ss}$ with "field-observation data".

Based on the values shown in Table 4, the values of $\gamma_{HNO_3,ss}$ were relaxed between 10^{-4} and 10^{-1} in this model sensitivity study. Figure 10 show the results of the sensitivity runs for the determination of $\gamma_{HNO_3,ss}$. As mentioned in Sect. 3.3, two (directly-

ACPD
9, 11699–11751, 2009

measured and estimated) HNO_3 concentrations were used in this analysis. Again, in order to evaluate the magnitude of $\gamma_{HNO_3,ss}$, two items were examined: (i) how close are the estimated HNO_3 concentrations to the directly-measured HNO_3 concentrations? and (ii) how close are the model-calculated HNO_3 concentrations to both observation-based HNO_3 concentrations? Among the results, this paper presents the data from three sensitivity model runs with $\gamma_{HNO_3,ss}=10^{-4}$, 10^{-3}, and 5×10^{-3} in Fig. 10, because these model sensitivity runs show the best comparison results. The following occurred if $\gamma_{HNO_3,ss}>5\times10^{-3}$ are used: (i) several estimated HNO_3 concentrations (black circles in Fig. 10) become smaller than the directly-measured HNO_3 concentrations (red circles in Fig. 10) and (ii) several estimated HNO_3 concentrations become <0. Both appear to be unreasonable. In addition, the comparisons at the plume transects A and B in Fig. 10 were excluded, because large discrepancies were already found in the previous analysis (refer to Fig. 7).

The estimated HNO_3 concentrations were generally higher than the model-predicted HNO_3 concentrations with $\gamma_{HNO_3,ss}=10^{-4}$ and 10^{-3}, as shown in Fig. 10, whereas the directly-observed HNO_3 concentrations were always lower than the model-predicted HNO_3 concentrations in all cases. The under-predictions of the HNO_3 concentrations at the plume transects C and D originated partly from the high levels of NO_y observed, as shown in Fig. 5. However, as the ship-plume ages, the simulation results with $\gamma_{HNO_3,ss}=10^{-4}$ and 10^{-3} approach the estimated HNO_3 concentrations, and the estimated HNO_3 concentrations also approach the directly-measured HNO_3 levels. At the fully developed ship-plume stages (transects E to H), the simulations with $\gamma_{HNO_3,ss}=5\times10^{-3}$ over-predict the HNO_3 concentrations, and the estimated HNO_3 concentrations begin to be smaller than the directly-measured HNO_3 concentrations. Based on these comparison, it was concluded that the magnitude of $\gamma_{HNO_3,ss}$ might be between 10^{-4} and 10^{-3}. However, further studies on the issue of $\gamma_{HNO_3,ss}$ will be necessary.

Here, another issue that can be raised is the role of ammonia (NH_3) in the heterogeneous conversion of HNO_3. In a typical urban atmosphere, HNO_3 partitioning into

ACPD
9, 11699–11751, 2009

"acidic" urban particles tends to accompany NH_3 condensation (Seinfeld and Pandis, 1998):

$$HNO_3 + NH_3 \leftrightarrow NH_4NO_3 \quad \text{(R8)}$$

NH_3 condensation imparts alkalinity to "acidic" urban particles for the HNO_3 partitioning (Seinfeld and Pandis, 1998; Song and Carmichael, 1999, 2001). However, in the case of alkaline aerosols, such as sea-salt and mineral dust, there is already sufficient alkalinity inside the particles, so that accompanying NH_3 condensation is not necessary. On the other hand, although HNO_3 partitioning accompanies NH_3 condensation, NH_3 would be vaporize immediately because partitioned NO_3^- thermodynamically favors an association with Na^+ or other inorganic cations inside the sea-salt particles rather than with NH_4^+ (Song and Carmichael, 1999; Song et al., 2005).

5 NO_x chemical lifetimes

A convenient way of examining the chemical evolution of pollution plumes is to quantify the NO_x chemical lifetimes. Several research groups (e.g., Sillman et al., 1990; Karamchandani et al., 1998; Ryerson et al., 1998, 2001; Sillman, 2000) examined the plume NO_x chemical lifetime to evaluate the chemical evolution of power-plant plumes. On the other hand, Lawrence and Crutzen (1999) examined the chemical lifetimes of NO_x emitted from ocean-going ships within the MBL, using an Eulerian 3-D photochemical model. However, the NO_x chemical lifetimes were overestimated because their modeling study bypassed the nonlinear ship-plume NO_x chemistry. In order to include the nonlinear ship-plume chemistry, von Glasow et al. (2003) and Song et al. (2003a) used a Lagrangian photochemical box model to estimate the NO_x chemical lifetimes more accurately. Their results clearly showed that the elevation of the plume OH concentrations reduces the NO_x chemical lifetime by a factor of 2.5~3.0. Nevertheless, their study had some limitations in that: (i) the estimations were made only along the plume centerline, where it is difficult to demonstrate/represent the chemical evolution of the

ACPD
9, 11699–11751, 2009

"entire volume" of the ship plume, and (ii) the model was used without adequate model verification. Here, the ship-plume NO_x chemical lifetimes were examined again using the newly developed ship-plume photochemical model, which can reflect the chemical aging of the entire ship-plume volume. The "instantaneous NO_x lifetime ($\tau^i_{NO_x}$)" defines how fast NO_x is lost at a given point of time. $\tau^i_{NO_x}$ is defined as the NO_x concentration at a given point of time divided by the rate of NO_x loss ($L^i_{NO_x}$) at a given time (Sillman, 2000; Song et al., 2003a; Chen et al., 2005; Han et al., 2009):

$$L^i_{NO_x} = k_1[OH][NO_2] + k_2[NO_3][DMS] + k_{mt,NO_3}[NO_3] + 2k_{mt,N_2O_5}[N_2O_5] + k_3[CH_3CO_3][NO_2] - (k_4 + J_1)[PAN] \quad (15)$$

$$\tau^i_{NO_x} = \frac{[NO] + [NO_2]}{L^i_{NO_x}} \quad (16)$$

where k_1, k_2, k_3, and k_4 are the thermal reaction rate coefficients; k_{mt,NO_3} and k_{mt,N_2O_5} are the mass transfer coefficients (s^{-1}) for the heterogeneous conversion of atmospheric NO_3 and N_2O_5 radicals, respectively (refer to Eqs. 1 and 2); and J_1 is the photo-dissociation rate coefficient of PAN.

A "moderately stable" condition was assumed in the estimations of $\tau^i_{NO_x}$. The estimated results are presented in Fig. 11. Panels a–h in Fig. 11 correspond sequentially to plume transects A–H. Because the overall rate of NO_x loss in Eq. (15) is controlled mainly by the NO_2+OH reaction, the OH radical concentrations (dashed blue lines) tend to be inversely correlated with $\tau^i_{NO_x}$ (solid red lines) throughout the panels a–h in Fig. 11. Highly non-linear and non-Gaussian shape of the distribution in OH concentrations and $\tau^i_{NO_x}$ were observed at plume transect A. Such non-linear chemistry occurs not only "along the plume-advecting direction" (i.e., x-direction), but also "across the plume cross-section" (i.e., y- and z-directions). This is one of the main reasons why the development of entire-volume ship-plume model is necessary. After the plume transects A and B, both the OH concentrations and $\tau^i_{NO_x}$ have Gaussian shapes across the

ACPD
9, 11699–11751, 2009

plume cross-sections (C–H), with mirror-images of each other.

The averaged OH concentrations ($[\overline{OH}]$) and instantaneous $\tau^i_{NO_x}$ ($\overline{\tau^i_{NO_x}}$) across the plume cross-sections (A–H) are also shown inside the panels a–h in Fig. 11. In particular, $\overline{\tau^i_{NO_x}}$ was calculated, considering the distribution of NO_x concentrations, i.e.:

$$w_j = \frac{NO_x|_j}{\sum_{j=1}^{n} NO_x|_j} \quad (17)$$

$$\overline{\tau^i_{NO_x}} = \sum_{j=1}^{n} \tau^i_{NO_x}\Big|_j w_j \quad (18)$$

where w_j, $NO_x|_j$, and $\tau^i_{NO_x}\Big|_j$ represent the weight factor (or NO_x fraction), NO_x concentrations, and estimated instantaneous NO_x lifetime ($\tau^i_{NO_x}$) at the j^{th} bin of the NO_x distribution across a ship-plume cross-section, respectively. n is the total number of bins of the NO_x distribution across a ship-plume cross-section. The bins considered in this estimation ranged from $+3\sigma$ to -3σ. Figure 12 was drawn to show the changes in $[\overline{OH}]$ and $\overline{\tau^i_{NO_x}}$ along the ship-plume travel distances under the "moderately stable" condition. Here, there is highly non-linear ship-plume photochemistry along the "plume-advecting" direction (i.e., in the x-direction). The $[\overline{OH}]$ and $\overline{\tau^i_{NO_x}}$ along the plume-advecting direction also have mirror-image distributions. The estimated $\overline{\tau^i_{NO_x}}$ ranges from 2.30 to 3.16 (h), and $\overline{\tau^i_{NO_x}}$ averaged over entire ship-plume is 2.90 (h). In addition, $[\overline{OH}]$ ranges from 0.87×10^7 to 1.56×10^7 (# cm^{-3}). Since the measured background OH radical concentrations were 0.61×10^7 # cm^{-3}, the ship-plume OH concentrations were elevated by factors of 1.4 to 2.6 as a result of the ship-plume chemistry. On the other hand, if $\overline{\tau^i_{NO_x}}$

ACPD
9, 11699–11751, 2009

is compared with the observed background NO_x lifetime ($\tau^b_{NO_x}$) of ~6.5 h (Chen et al., 2005), it can be concluded that the nonlinear ship-plume chemistry shortens the NO_x chemical lifetimes by a factor of ~2.2. The instantaneous NO_x lifetime ($\overline{\tau^i_{NO_x}}$) averaged over the plume cross-sections were integrated further along the plume-advection direction (i.e., integration of $\overline{\tau^i_{NO_x}}$ along the red solid line shown in Fig. 12). This lifetime is called the "equivalent NO_x lifetime ($\tau^{eq}_{NO_x}$)", which can be calculated using the following formula (Chen et al., 2005):

$$\tau^{eq}_{NO_x} = \frac{\Delta t}{\int_{t}^{t+\Delta t} \overline{\tau^i_{NO_x}}} \quad (19)$$

where Δt denotes the estimation period of chemical evolution. The value of $\tau^{eq}_{NO_x}$ estimated by Eq. (19) from the plume transects A to H (i.e., Δt=135 min) is 2.79 h. $\tau^{eq}_{NO_x}$ of 2.79 h is quite close to the simply averaged $\overline{\tau^i_{NO_x}}$ of 2.90 h. Again, the non-linear ship-plume chemistry shortens the NO_x lifetime considerably. $\tau^{eq}_{NO_x}$ was evaluated further from the "location of the ship stack" (i.e., travel distance x=0) to the approximate plume ending point (i.e., x=180 km) $\tau^{eq}_{NO_x}$ was estimated to be ~3.36 h because the early plume development stage has a relatively longer NO_x lifetime.

The lifetimes of 3.36 h are rather smaller than that used by Beirle et al. (2004) ($\tau^{eq}_{NO_x}$=3.70 h at 10:30 a.m. LST, the GOME passing local time). The accurate estimation of ship NO_x lifetime is of primary importance, particularly in the estimation of NO_x emissions from ocean-going ships using satellite NO_2 columns, as carried out by Beirle et al. (2004). Furthermore, the NO_x lifetimes inferred from this study are larger than those reported by Chen et al. (2005) ($\tau^{eq}_{NO_x}$=1.81–2.38 h). On the other hand, the lifetimes from this study can be compared with those from power plant plume studies. Nunnermacker et al. (2000) reported NO_x lifetimes of 2.8–4.2 h. NO_x lifetime study of a

ship plume can also be important, particularly when satellite-derived NO_2 columns are compared with 3-D chemistry-transfer model-predicted NO_2 columns for large-scale point sources, such as power plants (e.g., Kim et al., 2006; Han et al., 2009).

6 General characteristics of ship-plume chemical evolution

Sections 3 to 5 evaluated the performance of the newly developed ship-plume photochemical model, and examined the chemical evolution of ship plumes. However, the discussions were mainly of the measured five ship-plume species (NO_x, NO_y, O_3, HNO_3, and H_2SO_4) and the estimated OH radical concentrations. This section investigates the more general characteristics of the ship-plume chemical evolution. To do so, the ship-plume photochemical model was allowed to analyze the concentrations of ten major species. Figure 13 shows the changes in the concentrations of those species. Here, the open circles and bars represent the observed average concentrations and concentrations at $\pm\sigma$ at the eight transects, respectively. Both the solid and dashed lines represent the transect-averaged species concentrations calculated from the ship-plume photochemical model under moderately stable (E) and stable (F) conditions, respectively.

In Fig. 13b and i, as ship-plume develops, the concentrations of the primary pollutants, such as NO_x and SO_2, decrease almost exponentially due to dilution and chemical transformations. The changes in NO_y tend to follow the trends of NO_x, as shown in panels b and c, because the major constituent of NO_y is NO_x. On the other hand, ozone is titrated due to the excessive NO levels via Reaction (R2) near the ship stack (or during the early plume development stage), which is then recovered via Reactions (R3) and (R4) as the NO_x concentration decreases. Figure 13a shows the dynamics and non-linear characteristics. Because the main source of OH radicals is ozone, the level of OH productions was also suppressed by ozone titration. However, as ozone is recovered, the OH radical concentrations are also recovered via Reactions (R9) and (R10)

ACPD
9, 11699–11751, 2009

as shown in Fig. 13h:

$O_3 + hv \rightarrow O(^1D) + O_2$ (R9)

$O(^1D) + H_2O \rightarrow 2OH$ (R10)

When ozone depletion occurs, the OH concentration decreases to almost 0 (note, plume aging time of 0 in Fig. 13h was around 11:00 a.m. LST). However, the OH concentration increases as the ozone is recovered, reaching a maximum level around noon. After that, its concentration decreases again. The hydroxyl radical (OH) is the major oxidant in the atmosphere. Its atmospheric oxidation reactions produce two reservoir species in both the N- and S-cycles: HNO_3 and H_2SO_4. As mentioned previously, there are discrepancies between the observed and model-predicted HNO_3 and H_2SO_4 concentrations at the early plume-development stages. However, there is a decrease in the differences between the model-predicted and observed HNO_3 and H_2SO_4 concentrations as the plume ages photochemically. Since both the HNO_3 and H_2SO_4 concentrations are controlled by the OH concentrations, their concentrations decrease after noontime. Figure 13e and f shows the changes in the nighttime species, N_2O_5 and NO_3. Although N_2O_5 and NO_3 are nighttime species, the excessive NO_2 concentrations increase the levels of these nighttime species to almost several pptv levels, even during the daytime. This type of phenomena was reported previously by Song et al. (2003a).

In general, the model-simulation results show good agreement with the observed concentrations. As mentioned previously, the turbulent dispersion is governed mainly by the atmospheric stability class. Therefore, the model-simulated primary species concentrations (NO_x and SO_2) in the "stable" condition are usually higher than those in the "moderately stable" condition. However, this is not always the case for secondary species because the ship-plume chemistry is highly non-linear. Moreover, the trends are reversed during the ship-plume development stages if one examines the changes in the ozone, OH, NO_3 and PAN concentrations (see Fig. 10e–h).

7 Conclusions

In this study, the photochemical ship-plume model was developed to make a better understanding of the chemical evolution processes of a ship plume. In particular, to simulate the chemical evolution of the "entire volume" of the ship plume, the concentration distribution of the primary pollutants, such as NO_x and SO_2, were assumed to have Gaussian distributions. Being driven by the Gaussian-distributed primary pollutants, the newly developed photochemical ship-plume model provides information on the chemical evolution of the ship-plume.

The simulation performance of the newly developed ship-plume model was evaluated by a comparison with the data obtained from a ship-plume measurement experiment carried out around noon on 8 May 2002 by a NOAA WP-3D aircraft. The model-simulation conditions were obtained directly and/or inferred indirectly from the NOAA WP-3D observations. In particular, the atmospheric stability conditions were estimated, analyzing the temperature profiles measured or obtained from the WP-3D aircraft observations and NCEP reanalysis data. Based on the analysis, it was determined that the likely stability class within the MBL would be between the "moderately stable" and "stable" conditions. The primary pollutant concentrations, such as NO_x and SO_2, always showed higher values in the "stable" condition than in the "moderately stable "condition. In contrast, due to the non-linear ship-plume chemistry, the concentrations of the secondary pollutants, such as O_3, OH, and NO_3, are higher in the moderately stable condition during the early ship-plume development stage. Correlation analysis between the observed and model-predicted ship-plume concentrations was carried out to analyze the model-simulation performances in more detail. The results from the moderately stable condition showed stronger correlations than those from the stable condition. In addition, the results from statistical analysis showed that the simulations under moderately stable condition produced concentrations closer to the observed ship-plume concentrations than under the stable condition.

The magnitude of the reaction probability of HNO_3 onto sea-salt particles ($\gamma_{HNO_3,ss}$)

ACPD
9, 11699–11751, 2009

was also investigated. From the study, it was concluded that the magnitude of $\gamma_{HNO_3,ss}$ might be in the order of 10^{-3} or smaller. In addition, the equivalent NO_x lifetimes throughout the "entire" plume were also estimated from ship-plume photochemical modeling. The chemical NO_x lifetime throughout the "entire ship plume" was estimated to be 3.36 h. This results clearly show that an increase in the levels of atmospheric oxidants in the ship plumes reduce the chemical lifetime of NO_x within the MBL by a factor of 2.5∼3.0.

On the other hand, Russell et al. (1999) examined the effect of ship-emitted aerosols on the cloud properties in a "ship track" using both an aerosol microphysical model, which can consider condensational and coagulational growth, and a cloud microphysics model. In their study, the Monterey Area Ship Track (MAST) experiment data, which had been measured in almost the same area where the WP-3D aircraft observations were made, had been used. However, although their study employed detailed aerosol microphysical and cloud microphysics models, it was limited in that (i) the model study did not consider the highly non-linear ship plume chemistry, and (ii) it did not account for the ship-plume dilution processes, and therefore the entrainment processes of the background air into the ship-plume volume. However, such limitations can be overcome if the developed ship-plume photochemical model is used. Therefore, it is expected that the combination of both detailed aerosol microphysical and cloud microphysics models with the ship-plume photochemical model shown in this study would allow more detailed ship track investigations in the future.

Acknowledgements. This study was funded by the Korea Ministry of Environment as an Ecotechnopia 21 project under grant 212-071-050, and was also supported by the basic research project through a grant provided by the Gwangju Institute of Science & Technology in 2009. Authors used all the ITCT 2K2 airborne data sets from the FTP server at the University of Iowa.

References

Abbatt, J. P. D. and Waschewsky, G. C. G.: Heterogeneous interactions of HOBr, HNO_3, O_3, and NO_2 with deliquescent NaCl aerosols at room temperature, J. Phys. Chem. A, 102, 3719–3725, 1998.

Atkinson, R., Baulch, D. L., Cox, R. A., Hampson Jr., R. F., Kerr, J. A., Rossi, M. J., and Troe, J.: Evaluated kinetic and photochemical data for atmospheric chemistry: Supplement V IUPAC Subcommittee on gas kinetic data evaluation for atmospheric chemistry, J. Phys. Chem. Ref. Data, 26(2), 215–280, 1997.

Beirle, S., Platt, U., von Glasow, R., Wenig, M., and Wanger, T.: Estimation of nitrogen oxide emission from shipping by satellite remote sensing, Geophys. Res. Lett., 31, L18102, doi:10.1029/2004GL020312, 2004.

Brasseur, G. P., Orlando, J. J., and Tyndall, G. S.: Atmospheric Chemistry and Global Change, Oxford University Press, New York, USA, 1999.

Brock, C. A., Schröder, F., Kärcher, B., Petzold, A., Busen, R., and Fiebig, M.: Ultrafine particle distributions measured in aircraft exhaust plumes, J. Geophys. Res., 105(D21), 26555–26567, 2000.

Brock, C. A., Trainer, M., Ryerson, T. B., Neuman, J. A., Parrish, D. D., Holloway. J. S., Kicks Jr., D. K., Frost, G. J., Hübler, G., Fehsenfeld, F. C., Wilson, J. C., Reeves, J. M., Lafleur, B. G., Hilbert, H., Atlas, E. L., Donnelly, S. G., Schauffler, S. M., and Stroud, V. R.: Particle growth in urban and industrial plumes in Texas, J. Geophys. Res., 108(D3), 4111, doi:10.1029/2002JD002746, 2003.

Capaldo, K., Corbett, J. J., Kasibhatla, P., and Pandis, S. N.: Effects of ship emissions on sulphur cycling and radiative climate forcing over the ocean, Nature, 400, 743–746, 1999.

Chen, G., Huey, L. G., Trainer, M., Nicks, D., Corbett, J., Ryerson, T., Rarrish, D., Neuman, J. A., Nowak, J., Tanner, D., Holloway, J., Brock, C., Crawford, J., Olson, J. R., Sullivan, A., Weber, R., Schauffler, S., Donnelly, S., Atlas, E., Roberts, J., Flocke, F., Hübler, G., and Fehsenfeld, F.: An investigation of the chemistry of ship emission plumes during ITCT 2002, J. Geophys. Res., 110, D10S90, doi:10.1029/2004JD005236, 2005.

Corbett, J. J. and Fishbeck, P.: Emission from ships, Science, 278(5339), 823–824, 1997.

Corbett, J. J., Fischbeck, P. S., and Pandis, S. N.: Global nitrogen and sulfur inventories for ocean-going ships, J. Geophys. Res., 104(D13), 16255–16273, 1999.

Corbett, J. J. and Koehler, H. W.: Updated emission form ocean shipping, J. Geophys. Res.,

108(D20), 4650, doi:10.1029/2003JD003751, 2003.
Crawford, J., Davis, D., Olson, J., Chen, G., Liu, S., Gregory, G., Barrick, J., Sachse, G., Sandholm, S., Heikes, B., Singh, H., and Blake, D.: Assessment of upper tropospheric HO_x sources over the tropical pacific based on NASA GTE/PEM data: Net effect on HO_x and other photochemical parameters, J. Geophys. Res., 104(D13), 16255–16273, 1999.
Davis, J. A. and Cox, R. A.: Kinetics of the heterogeneous reaction of HNO_3 with NaCl: Effect of water vapor, J. Phys. Chem. A, 102, 7631–7642, 1998.
Davis, D. D., Grodzinsky, G., Kasibhatla, P., Crawford, J., Chen. G., Liu, S., Bandy, A., Thornton, D., Guan. H., and Sandholm, S.: Impact of ship emissions on marine boundary layer NO_x and SO_2 distributions over the Pacific Basin, Geophys. Res. Lett., 28(2), 235–238, 2001.
DeMore, W. B., Sander, S. P., Golden, D. M., Hampson, R. F., Kurylo, M. J., Howard, C. W., Ravishankara, A. R., Kolb, C. E., and Molina, M. J.: Chemical kinetics and photochemical data for use in stratospheric modeling, Evaluation Number 12, JPL Publ., 97-4, 1997.
Endresen, Ø., Sørgård, E., Sundet, J. K., Dalsøren, S. B., Isaksen I. S. A., Berglen, T. F., and Gravir, G.: Emission from international sea transportation and environmental impact, J. Geophys. Res., 108(D17), 4560, doi:10.1029/2002JD002898, 2003.
Fenter, F. F., Caloz, F., and Rossi, M. J.: Kinetics of nitric acid uptake by salt, J. Phys. Chem., 98, 9801–9810, 1994.
Ferek, R. J., Hegg, D. A., Hobbs, P. V., Durkee, P., and Nielsen, K.: Measurements of ship-induced tracks in clouds off the Washington coast, J. Geophys. Res., 103(D18), 23199–23206, 1998.
Finlayson-Pitts, B. J. and Pitts Jr., J. N.: Chemistry of the upper and lower atmosphere, Academy Press, San Diego, California, USA, 570–573, 2000.
Ghosal, S. and Hemminger, J. C.: Surface adsorbed water on NaCl and its effect on nitric acid reactivity with NaCl powders, J. Phys. Chem. B, 108, 14102–14108, 2004.
Gill, A. E.: Atmosphere-Ocean Dynamics, Academic Press, p. 12, 1982.
Guimbaud, C., Arens, F., Gutzwiller, L., Gäggeler, H. W., and Ammann, M.: Uptake of HNO_3 to deliquescent sea-salt particles: a study using the short-lived radioactive isotope tracer ^{13}N, Atmos. Chem. Phys., 2, 249–257, 2002, http://www.atmos-chem-phys.net/2/249/2002/.
Han, K. M., Song, C. H., Ahn, H. J., Park, R. S., Woo, J. H., Lee, C. K., Richter, A., Burrows, J. P., Kim, J. Y., and Hong, J. H.: Investigation of NOx emissions and NOx-related chemistry in East Asia using CMAQ-predicted and GOME-derived NO_2 columns, Atmos. Chem. Phys.,

9, 1017–1036, 2009,
http://www.atmos-chem-phys.net/9/1017/2009/.
Hanna, S. R., Schulman, L. L., Paine, R. J., Pleim, J., and Baer, M.: Development and evaluation of the offshore and coastal dispersion model, J. Air Pollut. Control Assoc., 35, 1039–1047, 1985.
Hewitt, C. N.: The atmospheric chemistry of sulphur and nitrogen in power station plumes, Atmos. Environ., 35(7), 1155–1170, 2001.
Hobbs, P. V., Garrett, T. J., Ferek, R. J., Strader, S. R., Hegg, D. A., Frick, G. M., Hoppel, W. A., Gasparovic, R. F., Russell, R. M., Johnson, D. W., O'Dowd, C., Durkee, P. A., Nielsen, K. E., and Innis, G.: Emissions from ships with respect to their effects on clouds, J. Atmos. Sci., 57(16), 2570–2590, 2000.
Holton, J. R.: An Introduction to Dynamic Meteorology, Academic Press, 290 pp., 1992.
Hudson, J. G., Garrett, T. J., Hobbs, P. V., Strader, S. R., Xie, Y., and Yum, S. S.: Cloud condensation nuclei and ship tracks, J. Atmos. Sci., 57(16), 2696–2706, 2000.
Huey, L. C., Tanner, D. J., Slusher, D. L., Dibb, J. E., Arimoto, R., Chen, G., Davis, D., Buhr, M. P., Nowak, J. B., Mauldin III, R. L., Eisele, F. L., and Kosciuch, E.: CIMS measurements for HNO_3 and SO_2 at the South Pole during ISCAT 2000, Atmos. Environ., 38(32), 5411–5421, 2004.
Jefferson, A., Eisele, F. L., Ziemann, P. J., Weber, R. J., Marti, J. J., and McMurry, P. H.: Measurements of the H_2SO_4 mass accommodation coefficient onto polydisperse aerosol, J. Geophys. Res., 102, 19021–19028, 1997.
Karamchandani, P., Koo, A., and Seigneur, C.: Reduced gas-phase kinetic mechanism for atmospheric plume chemistry, Environ. Sci. Technol., 32, 1709–1720, 1998.
Karamchandani, P., Santos, L., Sykes, I., Zhang, Y., Tonne, C., and Seigneur, C.: Development and evaluation of a state-of-the-science reactive plume model, Environ. Sci. Technol., 34, 870–880, 2000.
Kasibhatla, P., Levy II, H., Moxim, W. J., Pandis, S. N., Corbett, J. J., Peterson, M. C., Honrath, R. E., Forst, G. J., Knapp, K., Parrish, D. D., and Ryerson, T. B: Do emissions from ship have a significant impact on concentrations of nitrogen oxides in the marine boundary layer?, Geophys. Res. Lett., 27, 2229–2232, 2000.
Kim, S. W., Heckel, A., McKeen, S. A., Frost, G. J., Hsie, E. Y., Trainer, M. K., Richter, A., Burrows, J. P., Peckham, S. E., and Grell, G. A.: Satellite-observed U.S. power plant NO_x emission reductions and their impact on air quality, Geophys. Res. Lett., 33, L22812,

doi:10.1029/2006GL027749, 2006.
Nowak, J. B., Parrish, D. D., Neuman, J. A., Holloway, J. S., Cooper, O. R., Ryerson, T. B., Nicks Jr., D. K., Flocke, F., Roberts, J. M., Atlas, E., de Gouw, J. A., Donnelly, S., Dunlea, E., Hübler, G., Huey, L. G., Schauffler, S., Tanner, D. J., Warneke, C., and Fehsenfeld, F. C.: Gas-phase chemical characteristics of Asian emission plumes observed during ITCT 2K2 over the eastern North Pacific Ocean, J. Geophys. Res., 109, D23S19, doi:10.1029/2003JD004488, 2004.
Nunnermacker, L. J., Kleinman, L. T., Imre, D., Daum, P. H., Lee, Y.-N., Lee, J. H., Springton, S. R., Newman, L., and Gillani, N.: NO_y life times and O_3 production efficiencies in urban and power plant plumes: Analysis of field data, J. Geophys. Res., 105, 9165–9176, 2000.
Laux, J. M., Hemminger, J. C., and Finlayson-Pitts, B. J.: X-ray photoelectron spectroscopic studies of the heterogeneous reaction of gaseous nitric acid with sodium chloride: Kinetics and contribution to the chemistry of the marine troposphere, Geophys. Res. Lett., 21(15), 1623–1626, 1994.
Lawrence, M. G. and Crutzen, P. J.: Influence of NO_x emissions from ships on tropospheric photochemistry and climate, Nature, 402, 197–170, 1999.
Lui, Y., Cain, J. P., Wang, H., and Laskin, A.: Kinetic study of heterogeneous reaction of deliquesced NaCl particles with gaseous HNO_3 using particle-on-substrate stagnation flow reactor approach, J. Phys. Chem. A, 111, 10026–10043, 2007.
Lurmann, F., Lloyd, A., and Atkinson, R.: A chemical mechanism for use in long-range transport/acid deposition computer modeling, J. Geophys. Res., 91(D10), 10905–10936, 1986.
Mari, C., Suhre, K., Rosset, R., Bates, T. S., Huebert, B. J., Bandy, A. R., Thornton, D. C., and Businger, S.: One-dimensional modeling of sulfur during the First Aerosol Characterization Experiment (ACE 1) Lagrangian B, J. Geophys. Res., 104(D17), 21733–21749, 1999.
Orsini, D. A., Ma, Y., Sullivan, A., Sierau, B., Baumann, K., and Weber, R. J.: Refinements to the particle-into-liquid-sampler (PILS) for ground and airborne measurements of water-soluble aerosol composition, Atmos. Environ., 37(9–10), 1243–1259, 2003.
Parrish, D. D., Kondo, Y., Cooper, O. R., Brock, C. A., Jaffe, D. A., Trainer, M., Ogawa, T., Hübler, G., and Fehsenfeld, F. C.: Intercontinental Transport and Chemical Transformation 2002 (ITCT 2K2) and Pacific Exploration of Asian Continental Emission (PEACE) experiments: An overview of the 2002 winter and spring intensives, J. Geophys. Res., 109, D23S01, doi:10.1029/2004JD004980, 2004.
Phinney, L., Leaitch, W. R., Lohmann, U., Shantz, N. C., and Worsnop, D. R.: Contributions

from DMS and ship emissions to CCN observed over the summertime North Pacific, Atmos. Chem. Phys. Discuss., 9, 309–361, 2009, http://www.atmos-chem-phys-discuss.net/9/309/2009/.

Radke, L. F., Coakley, J. A., and King, M. D.: Direct and remote-sensing observations of the effects of ships on cloudes, Science, 246(4934), 1146–1149, 1989.

Russell, L. M., Seinfeld, J. H., Flagan, R. C., Ferek, R. J., Hegg, D. A., Hobbs, P. V., Wobrock, W. Flossmann, A. I., O'Dowd, C. D., Nielsen, K. E., and Durkee, P. A.: Aerosol dynamics in ship tracks, J. Geophys. Res., 104(D24), 31077–31095, 1999.

Ryerson, T. B., Buhr, M. P., Frost, G. J., Goldan, P. D., Holloway, J. S., Hübler, G., Jobson, B. T., Kuster, W. C., McKeen, S. A., Parrish. D. D., Roberts, J. M., Sueper, D. T., Trainer, M., Williams, J., and Fehsenfeld, F. C.: Emission lifetimes and ozone formation in power plant plume, J. Geophys. Res., 130(D17), 22569–11583, 1998.

Ryerson, T. B., Trainer, M., Holloway, J. S., Parrish, D. D., Huey, L. G., Sueper, D. T., Frost, G. J., Donnelly, S. G., Schauffler, S,. Atlas, E. L., Kuster, W. C., Goldan, P. D., Hübler, G., Meagher, J. F., and Fehenfeld, F. C.: Observation of ozone formation in power plant plume Implication for ozone control strategies, Science, 292(5517), 719–723, 2001.

Saul, T. D., Tolocka, M. P., and Johnston, M. V.: Reactive uptake of nitric acid onto sodium chloride aerosol across a wide range of relative humidities, J. Phys. Chem. A, 110, 7614–7620, 2006.

Schwartz, S. E: Mass-transport considerations pertinent to aqueous-phase reactions of gases in liquid-water clouds, in: Chemistry of Multiphase Atmospheric Systems, edited by: Jaeschke, W., Springer, Heidelberg, Germany, 415–471, 1986.

Seinfeld, J. H. and Pandis, S. N.: Atmospheric Chemistry and Physics: From Air Pollution to Climate Change, John Wiley and Sons, New York, USA, 1998.

Sillman, S., Logan, J. A., and Wofsy, S. C.: A regional scale model for ozone in the United States with subgrid representation of urban and power plant plumes, J. Geophys. Res., 95(D5), 5731–5748, 1990.

Sillman, S.: Ozone production efficiency and loss of NO_x in power plant plumes: Photochemical model and interpretation of measurements in Tennessee, J. Geophys. Res., 105(D7), 9189–9202, 2000.

Sinha, P., Hobbs, P. V., Yokelson, R. J., Christian, T. J., Kirchstetter, T. W., and Bruintjes, R.: Emissions of trace gases and particles from two ships in the southern Atlantic Ocean, Atmos. Environ., 37(15), 2139–2148, 2003.

Song, C. H. and Carmichael, G. R.: The aging processes of naturally-emitted aerosol (sea-salt and marine aerosol) during long range transport, Atmos. Environ., 33(14), 2203–2218, 1999.
Song, C. H. and Carmichael, G. R.: Gas-particle partitioning of nitric acid modulated by alkaline aerosol, J. Atmos. Chem., 40(1), 1–22, 2001.
Song, C. H., Chen, G., Hanna, S. R., Crawford, J., and Davis, D. D: Dispersion and chemical evolution of ship plumes in the marine boundary layer: Investigation of $O_3/NO_y/HO_x$ chemistry, J. Geophys. Res., 108(D4), 4143, doi:10.1029/2002JD002216, 2003a.
Song, C. H., Chen, G., and Davis, D. D.: Chemical evolution and dispersion of ship plumes in the remote marine boundary layer: Investigation of sulfur chemistry, Atmos. Environ., 37(19), 2663–2679, 2003b.
Song, C. H., Maxell-Meier, K., Rodney, R. J., Kapustin, V., and Clarke, A.: Dust composition and mixing state inferred from airborne composition measurements from ACE-Asia C130 Flight#6, Atmos. Environ., 39, 359–369, 2005.
Song, C. H., Han, K. M., Cho, H. J., Kim, J., Carmichael, G. R., Thongboonchoo, N., Kurata, G., Hem, Z., and Kim, H. S.: A Lagrangian model investigation of chemico-microphysical evolution of East Asian pollution plumes within the MBL during Trace-P, Atmos. Environ., 41(39), 8932–8951, 2007.
Talukdar, R. K., Gilles, M. K., Battin-Leclerc, F., Ravishankara, A. R., Fracheboud, J. M., Orlando, J. J., and Tyndall, G. S.: Photolysis of ozone at 308 nm and 248 nm: Quantum yield of O(1D) as a function of temperature, Geophys. Res. Lett., 24, 1091–1094, 1997.
Tolocka, M. P., Saul, T. D., and Johnston, M. V.: Reactive uptake of nitric acid into aqueous sodium chloride droplets using real-time single-particle mass spectrometry, J. Phys. Chem. A, 108, 2659–2665, 2004.
Tuttle, K. L.: Combustion-generated emissions in marine propulsion systems, in Proceedings of the SNAME 1994 Environmental Symposium – Ship Design and Operation in Harmony with the Environment, Soc. of Nav. Archit. and Mar. Eng., Jersey City, NJ, USA, 311–323, 1995.
Twomey, S.: Influence of pollution on shortwave albedo of clouds, J. Atmos. Sci., 34(7), 1149–1152, 1977.
von Glasow, R., Lawrence, M. G., Sander, R., and Crutzen, P. J.: Modeling the chemical effects of ship exhaust in the cloud-free marine boundary layer, Atmos. Chem. Phys., 3, 233–250, 2003,

http://www.atmos-chem-phys.net/3/233/2003/.
Weber, R. J., Orsini, D., Daun, Y., Lee, Y.-N., Klotz, P., and Brechtel, F.: A particle-in-liquid collector for rapid measurement of aerosol chemical composition, Aerosol Sci. Technol., 35(10), 718–727, 2001.
Worsnop, D. R., Zahniser, S., Kolb, C. E., Garner, J. A., Watson, L. R., van Doren, J. M., Jayne, J. T., and Davidovits, P.: The temperature dependence of mass accommodation of SO_2 and H_2O_2 on aqueous surfaces, J. Phys. Chem., 93, 1159–1172, 1989.

Table 1. Formulas for the later and vertical dispersion parameters, $\sigma_y(x)$ and $\sigma_z(x)$, as a function of the downwind distance, $x(m)$, over the ocean[a].

Pasquill stability class	σ_y (m)[b]	σ_z (m)
For x<10 km		
A	$0.11x(u/u_r)(1+0.0001\mathrm{x}(u/u_r))^{-1/2}$	$0.10x(u/u_r)$
B	$0.08x(u/u_r)(1+0.0001x(u/u_r))^{-1/2}$	$0.06x(u/u_r)$
C	$0.055x(u/u_r)(1+0.0001x(u/u_r))^{-1/2}$	$0.04x(u/u_r)(1+0.0002x(u/u_r))^{-1/2}$
D	$0.04x(u/u_r)(1+0.0001x(u/u_r))^{-1/2}$	$0.03x(u/u_r)(1+0.0015x(u/u_r))^{-1/2}$
E	$0.03x(u/u_r)(1+0.0001x(u/u_r))^{-1/2}$	$0.015x(u/u_r)(1+0.0003x(u/u_r))^{-1}$
F	$0.02x(u/u_r)(1+0.0001x(u/u_r))^{-1/2}$	$0.008x(u/u_r)(1+0.0003x(u/u_r))^{-1}$
For x>10 km		
A	$0.11x(u/u_r)(1+u/u_r)^{-1/2}$	$0.10x(u/u_r)$
B	$0.08x(u/u_r)(1+u/u_r)^{-1/2}$	$0.06x(u/u_r)$
C	$0.055x(u/u_r)(1+u/u_r)^{-1/2}$	$0.04x(u/u_r)(1+0.0002x(u/u_r))^{-1/2}$
D	$0.04x(u/u_r)(1+u/u_r)^{-1/2}$	$0.03x(u/u_r)(1+0.0015x(u/u_r))^{-1/2}$
E	$0.03x(u/u_r)(1+u/u_r)^{-1/2}$	$0.015x(u/u_r)(1+0.0003x(u/u_r))^{-1}$
F	$0.02x(u/u_r)(1+u/u_r)^{-1/2}$	$0.008x(u/u_r)(1+0.0003x(u/u_r))^{-1}$

[a] Here, u and u_r represent the wind speed and resulting wind speed, respectively.
[b] Because the standard deviation for lateral fluctuation in the turbulent velocity is not allowed to drop below 0.5 m s^{-1} (Hanna et al., 1985), the minimum value for σ_y is $0.5/u$.

ACPD
9, 11699–11751, 2009

Table 2. Simulation conditions used in this study.

Variables	Values
Emission rates	
NO_x (g/s)	6.25
SO_2 (g/s)	9.38
Meteorological conditions	
Sky condition	Clear sky
Stability class	Moderately stable (E), Stable (F)
Wind velocity (m/s)	9–11
Wind direction	SSE
Mixing height (m)[a]	800
Ship information	
Latitude (° N)	36.19
Longitude (° W)	123.06
Moving direction	WNW
Speed (knot)	9.7
Aerosol-related variables	
Background aerosol type	Sea-salt aerosols
Aerosol surface area ($\mu m^2/cm^3$)	90–120
$\gamma_{N_2O_5}$	0.1
γ_{NO_3}	0.01
$\gamma^{b}_{HNO_3}$	0.001
$\alpha^{c}_{SO_2}$	0.11
$\alpha^{d}_{H_2SO_4}$	0.79
Aerosol pH[e]	6.9
Background concentrations (ppbv)[f]	
[NO_x]	0.19
[O_3]	40
[CO]	138
[SO_2]	0.4
[C_3H_8]	0.37
[H_2SO_4]	0.0004
[HNO_3]	0.005
[PAN][g]	0.135

[a] Chen et al. (2005); [b] Sensitivity tests were made over the range of $\gamma_{HNO_3}=10^{-4}-10^{-1}$ (refer to Sect. 4 in this manuscript); [c] Worsnop et al. (1989); [d] Jefferson et al. (1997); [e] Assumed, based on Song et al. (2003b); [f] Obtained from WP-3D aircraft observations; also, refer to Chen et al. (2005); [g] Chen et al. (2005).

ACPD
9, 11699–11751, 2009

Table 3. Statistical analysis with observed and model-predicted plume concentrations at eight transects.

	Moderately Stable (E)				Stable (F)			
Species	RMSE[a]	MNGE[b]	MB[a]	MNB[b]	RMSE[a]	MNGE[b]	MB[a]	MNB[b]
NO_x	0.34	53.32	−0.20	−23.79	0.29	48.91	−0.09	−6.32
NO_y	0.51	54.79	−0.32	−23.43	0.43	37.42	−0.11	−1.43
O_3	0.92	1.90	−0.29	−0.63	0.93	1.82	−0.09	−0.16
HNO_3	0.17	68.24	−0.05	18.75	0.20	60.36	0.02	51.22
$H_2SO_4^c$	0.52	30.75	0.00	4.78	0.79	38.56	0.25	15.63

[a] Units are in ppbv, except for H_2SO_4.
[b] Units are in %.
[c] For H_2SO_4, the units for RMSE and NB are in pptv.

ACPD
9, 11699–11751, 2009

Table 4. Uptake coefficients of $HNO_3(g)$ onto NaCl and sea-salt particles.

Type of aerosol	Uptake coefficient, γ_{HNO_3}	D_p^a (μm)	RH (%)	Experimental Technique	Reference
NaCl, NaBr, KCl, and KBr	$(2.8\pm0.3)\times10^{-2}$	–	–	QMA[b]	Fenter et al. (1994)
NaCl	$(4\pm2)\times10^{-4}$	–	–	XPS[c]	Laux et al. (1994)
NaCl	>0.2	2–4	75	CIMS[d]	Abbatt and Waschewsky (1998)
NaCl	$(0.28–1.10)\times10^{-4}$	–	75	Mass spectrometer	Davis and Cox (1998)
Sea-salt	0.5 ± 0.2	~0.07	55	N^{13} isotope tracer	Guimbaud et al. (2002)
NaCl	$(5.25\pm3)\times10^{-3}$	1–10	–	XPS	Ghosal and Hemminger (2004)
NaCl	$(0.49–12.0)\times10^{-3}$	0.11–0.22	80	SPMS[e]	Tolocka et al. (2004)
NaCl and $NaCl/MgCl_2$	$(0.23–1.26)\times10^{-1}$	0.10–0.233	10–85	SPMS	Saul et al. (2006)
NaCl, $NaCl/MgCl_2$, and Sea-salt	~0.02	1.1–3.4	20–80	CCSEM/EDX[f]	Lui et al. (2007)

[a] D_p represents the aerodynamic diameter of a particle;
[b] Quandrupole Mass Analyzer;
[c] X-ray Photoelectron Spectroscopy;
[d] Chemical Ionization Mass Spectrometer;
[e] Single Particle Mass Spectrometer;
[f] Computer-controlled Scanning Electron Microscopy coupled with Energy-dispersed X-ray.

ACPD
9, 11699–11751, 2009

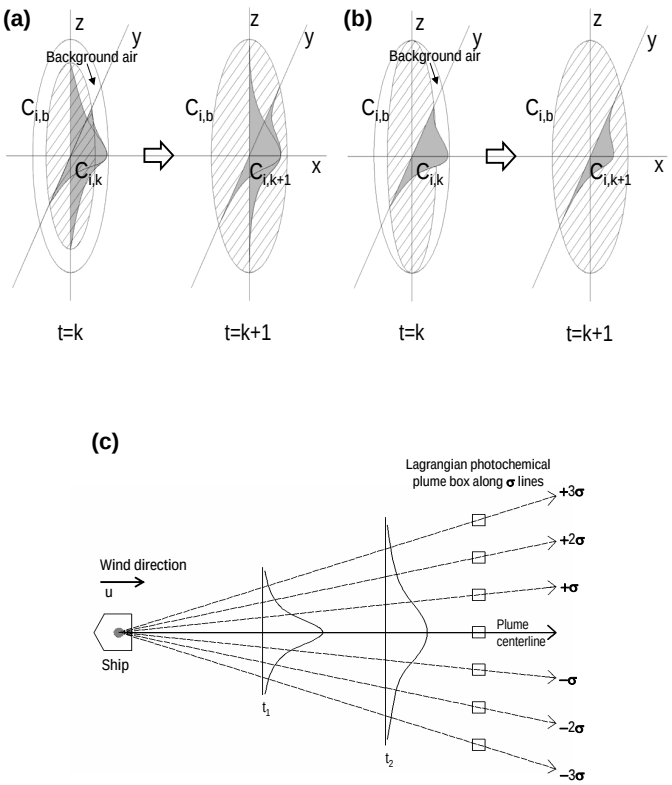

Fig. 1. Schematic diagram of ship-plume dispersion, **(a)** when σ_z<0.8 h and **(b)** when σ_z>0.8 h. **(c)** The illustration is shown for multiple Lagrangian ship-plume photochemical box runs.

ACPD
9, 11699–11751, 2009

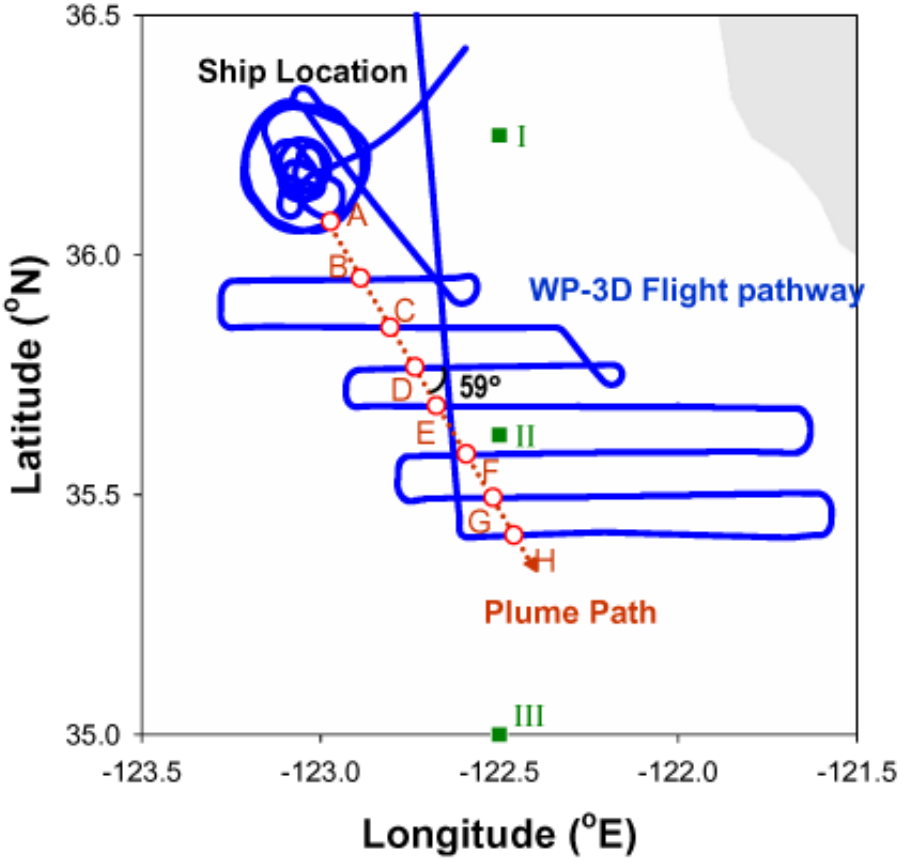

Fig. 2. Eight ship-plume transects (A–H) made by NOAA WP-3D flight near the California coast (Chen et al., 2005). I, II, and III denote three locations where the NCEP reanalysis data were obtained.

ACPD
9, 11699–11751, 2009

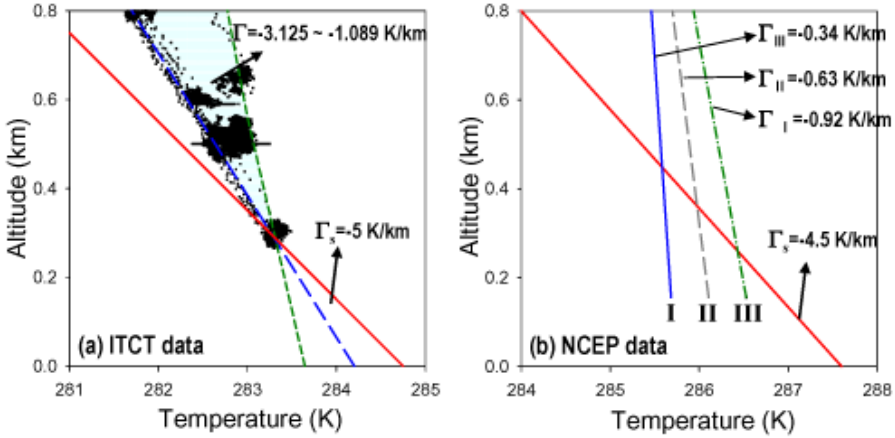

Fig. 3. Comparison between actual lapse rate (Γ and adiabatic lapse rate (Γ_s) for the determination of stability class of the MBL **(a)** with observations measured by NOAA WP-3D flight and **(b)** with NCEP 6 hourly reanalysis-2 pressure level data.

ACPD
9, 11699–11751, 2009

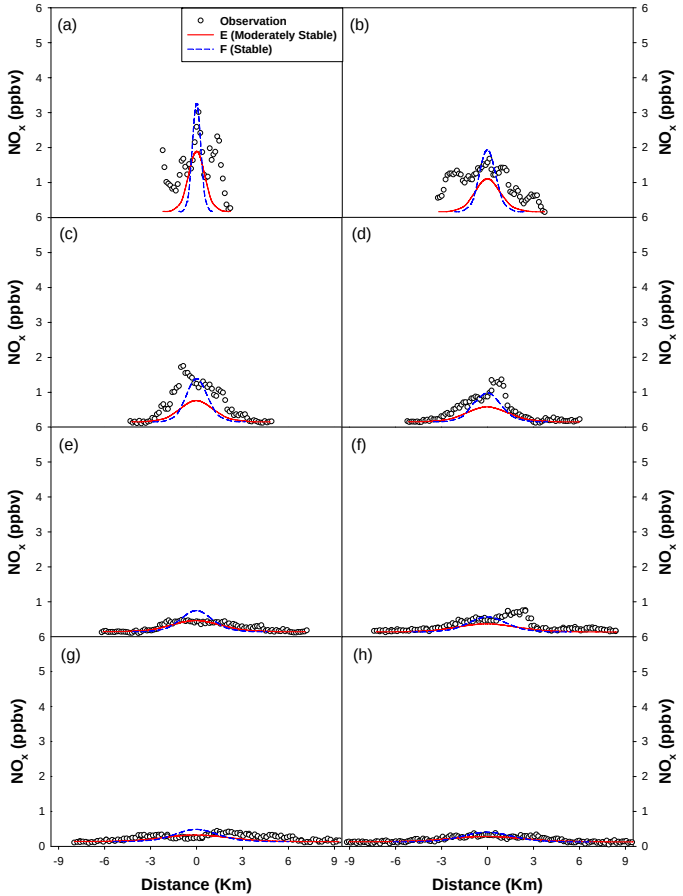

Fig. 4. Model-predicted vs. observed NO_x concentrations across the eight ship-plume transects (A–H) under the stability classes of "moderately stable (E)" and "stable (F)". Panels **(a–h)** correspond to the comparison at the ship-plume transects A–H, sequentially.

ACPD
9, 11699–11751, 2009

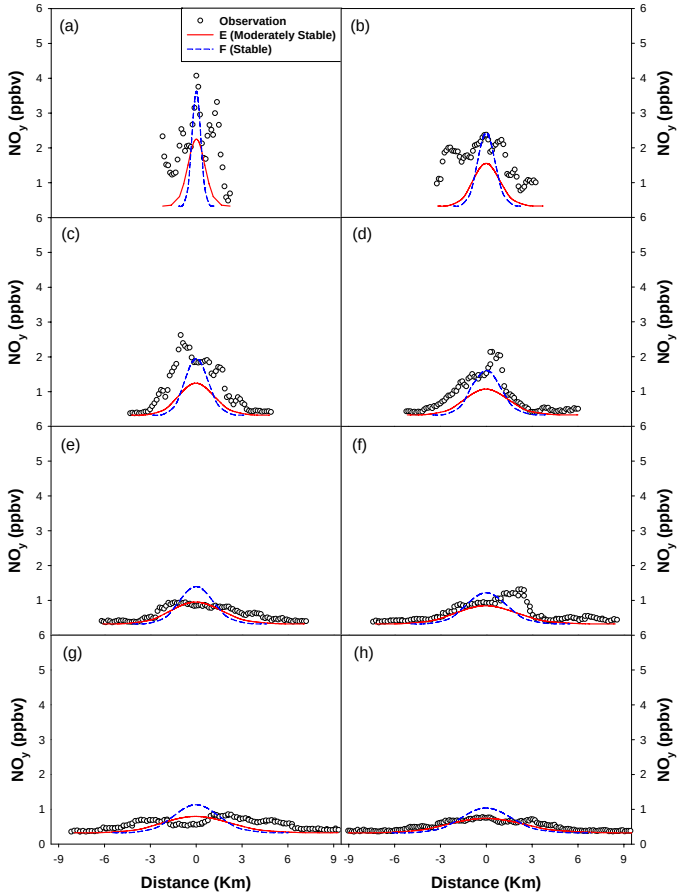

Fig. 5. As Fig. 4, except for NO_y.

ACPD
9, 11699–11751, 2009

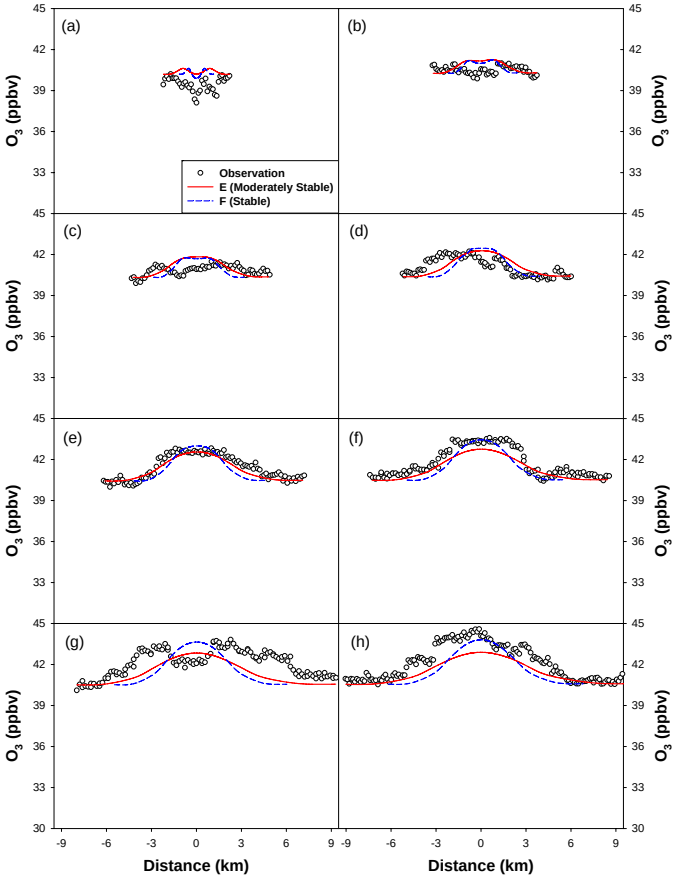

Fig. 6. As Fig. 4, except for O_3.

ACPD
9, 11699–11751, 2009

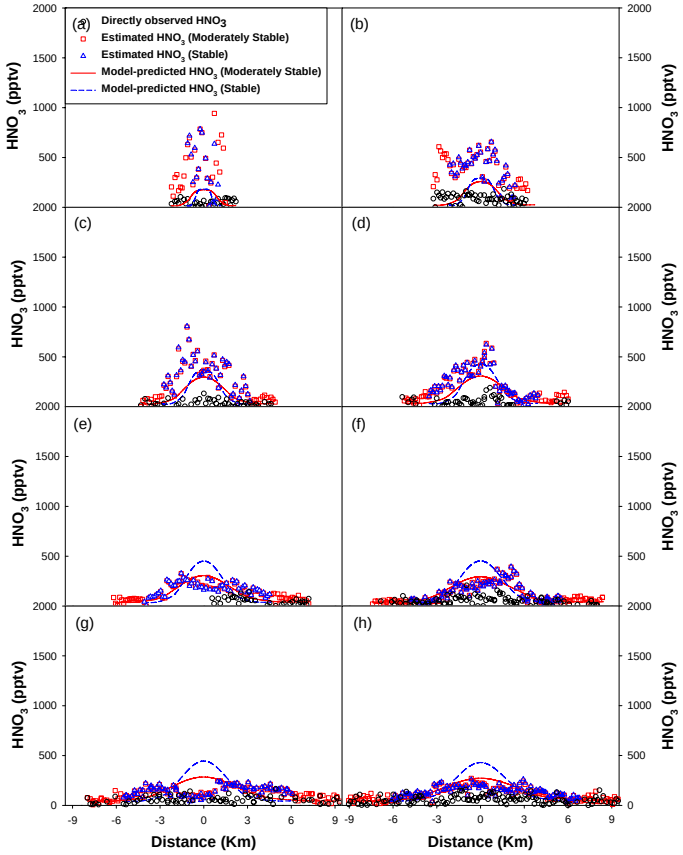

Fig. 7. As Fig. 4, except for HNO_3. $\gamma_{HNO_3,ss}$ of 10^{-3} was used in this study.

ACPD
9, 11699–11751, 2009

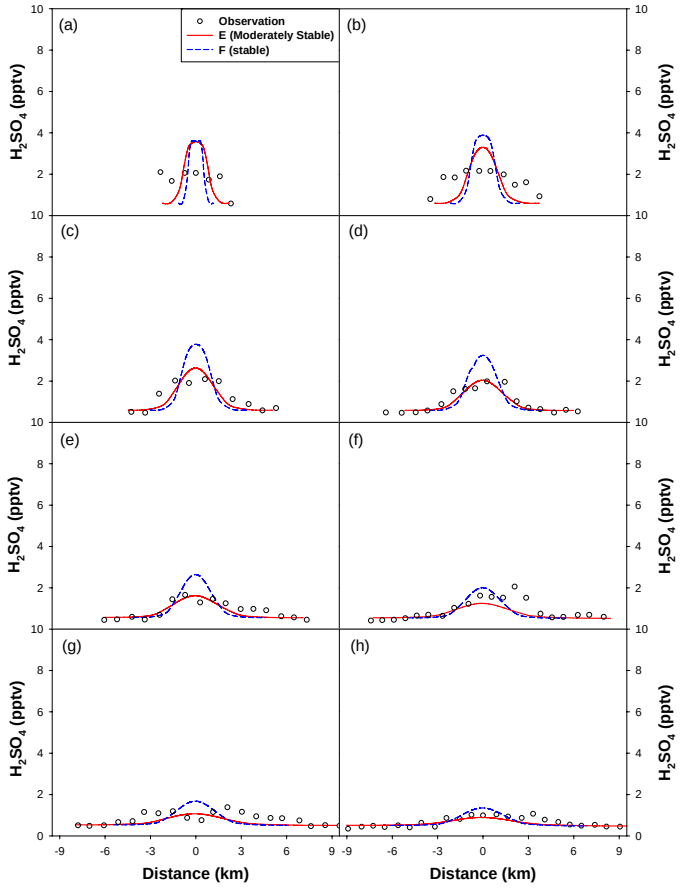

Fig. 8. As Fig. 4, except for H_2SO_4.

ACPD
9, 11699–11751, 2009

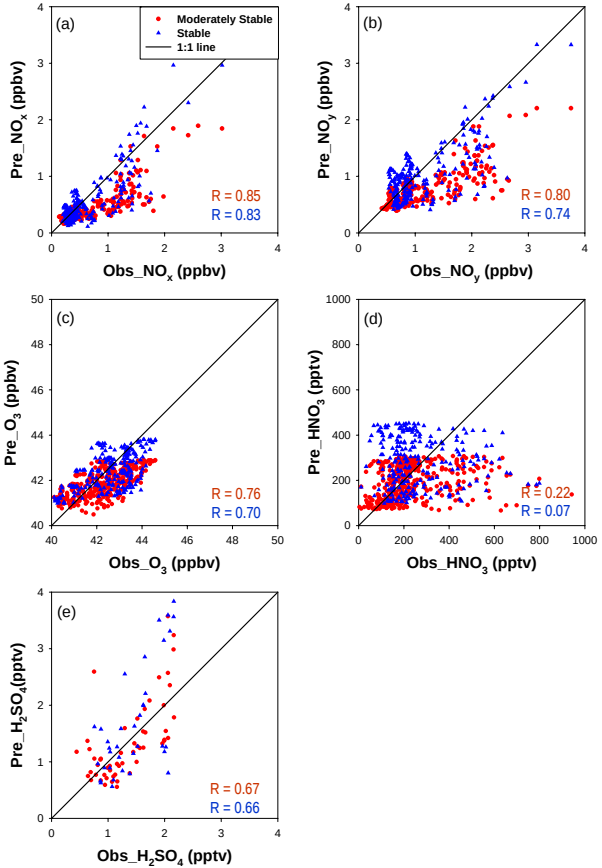

Fig. 9. Scatter plots of observed and model-predicted ship-plume concentrations: **(a)** NO_x; **(b)** NO_y; **(c)** O_3; **(d)** HNO_3; **(e)** H_2SO_4. The red circles and blue triangles represent the concentrations predicted by the ship-plume photochemical model under moderately stable and stable conditions, respectively. For HNO_3, the estimated HNO_3 concentrations were used in panel (d).

ACPD
9, 11699–11751, 2009

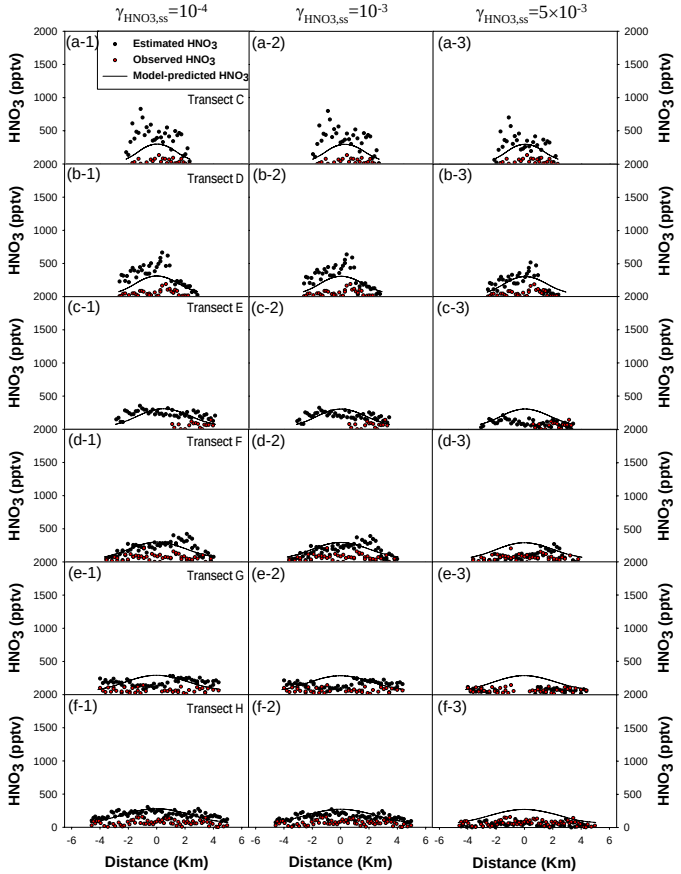

Fig. 10. Sensitivity tests for determining the reaction probability of HNO_3 into sea-salt particles ($\gamma_{HNO_3,ss}$). $\gamma_{HNO_3,ss}$ was relaxed from 10^{-4} to 5×10^{-3}. The first, second, and third columns represent the comparison results with $\gamma_{HNO_3,ss}=10^{-4}$, 10^{-3}, and 5×10^{-3}, respectively, at transects C to H.

ACPD
9, 11699–11751, 2009

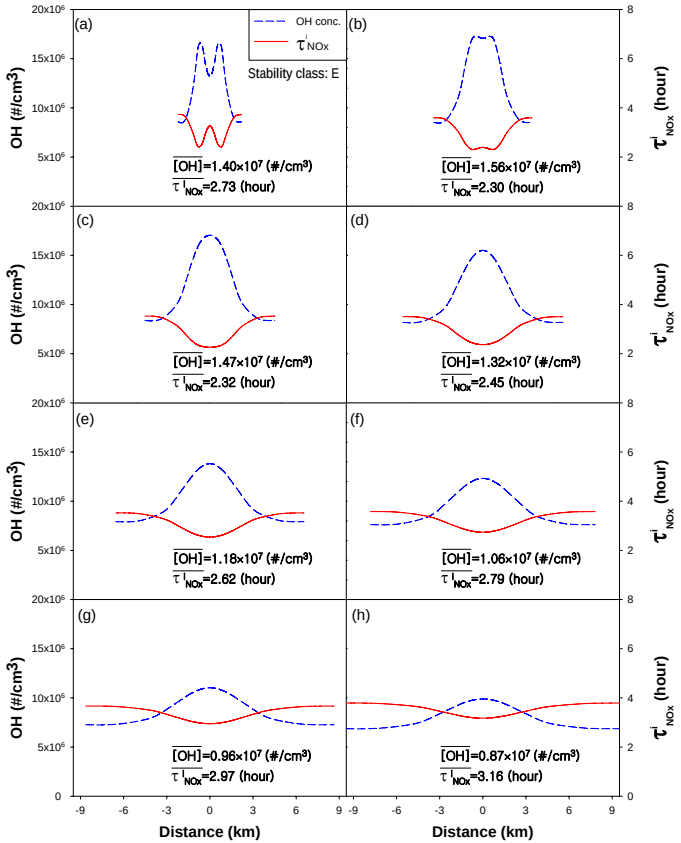

Fig. 11. OH radical concentrations and NO_x lifetimes across the ship-plume transects A–H. $[\overline{OH}]$ and $[\overline{\tau^{i}_{NO_x}}]$ represent the averaged OH concentration and instantaneous NO_x lifetime over the ship-plume transects A–H, respectively. UBoM 2K8 models were run at the stability condition of "moderately stable (E)". The panels **(a–h)** correspond to the results at the ship-plume transects A–H, sequentially.

ACPD
9, 11699–11751, 2009

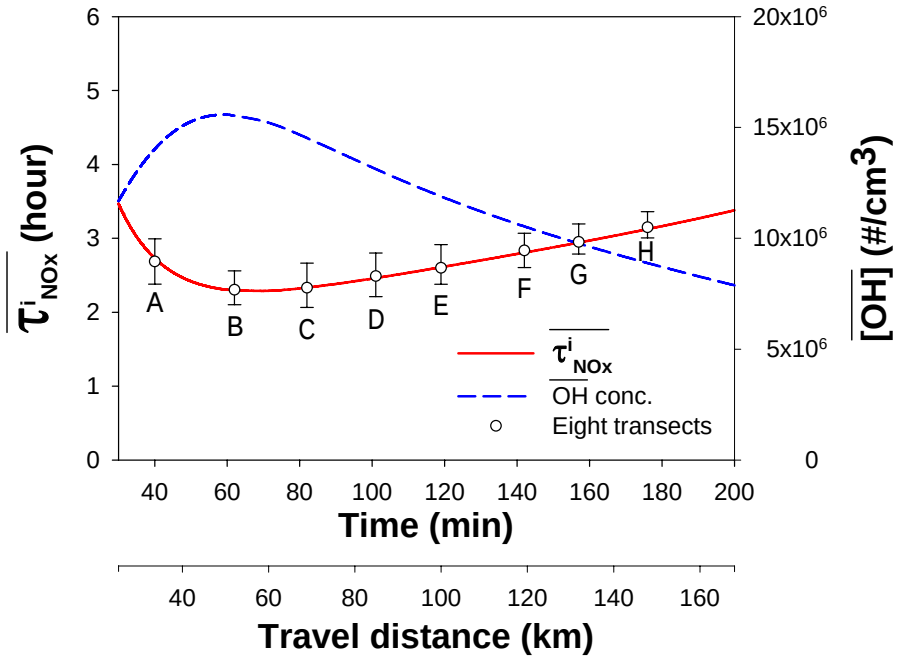

Fig. 12. Changes in $[\overline{OH}]$ and $[\overline{\tau^{i}_{NO_x}}]$ along the ship-plume travel distances under the stability condition of "moderately stable (E)". The bars represent the OH radical concentrations at $\pm\sigma$ in the eight ship-plume transects A–H.

ACPD
9, 11699–11751, 2009

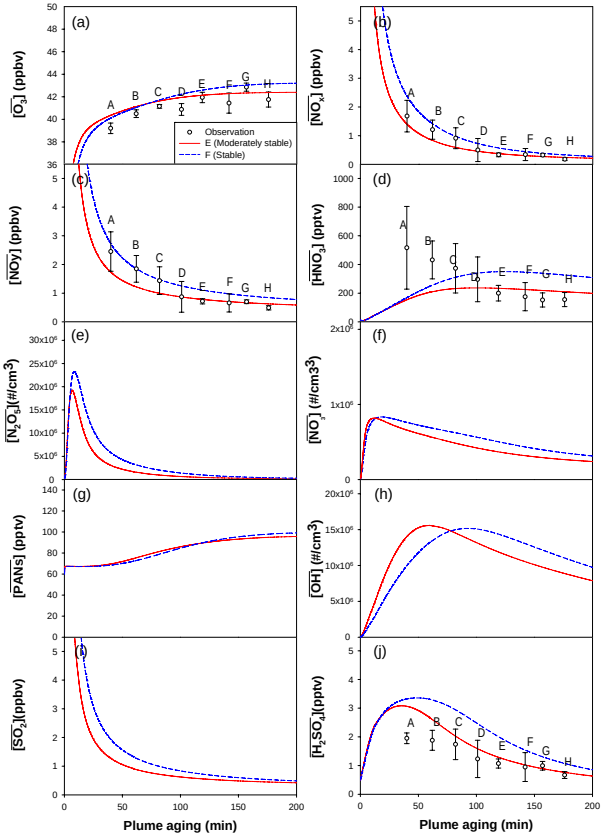

Fig. 13. Changes in ten major ship-plume species concentrations along the ship-plume travel times: **(a)** O_3; **(b)** NO_x; **(c)** NO_y; **(d)** HNO_3; **(e)** N_2O_5; **(f)** NO_3; **(g)** PANs; **(h)** OH; **(i)** SO_2; (*j*) H_2SO_4. The open circles and bars represent the observed average concentrations and concentrations at $\pm\sigma$. Here, the model runs were carried out with the stability class of "moderately stable (E)" and "stable (F)".

ACPD
9, 11699–11751, 2009